Science Advances
AAAS

advances.sciencemag.org/cgi/content/full/5/4/eaav2589/DC1

Supplementary Materials for

Super-elasticity of three-dimensionally cross-linked graphene materials all the way to deep cryogenic temperatures

Kai Zhao, Tengfei Zhang, Huicong Chang, Yang Yang, Peishuang Xiao, Hongtao Zhang, Chenxi Li, Chandra Sekhar Tiwary, Pulickel M. Ajayan*, Yongsheng Chen*

*Corresponding author. Email: yschen99@nankai.edu.cn (Y.C.); ajayan@rice.edu (P.M.A.)

Published 12 April 2019, *Sci. Adv.* **5**, eaav2589 (2019)
DOI: 10.1126/sciadv.aav2589

The PDF file includes:

Other Supplementary Material for this manuscript includes the following:

(available at advances.sciencemag.org/cgi/content/full/5/4/eaav2589/DC1)

Supplementary Methods

1. Atomic Force Microscopy (AFM) characterization was obtained on a Multimode 8 (Bruker Cooperation) using the ScanAsyst mode.

2. Thermal expansion measurement

The investigated 3DGraphene foam sample was 15 × 6 × 6 mm^3 cuboid. A thermal mechanical analyzer (TMA/SS6300, Seiko Instruments, Japan) was used to measure the thermal expansion between 4 K and 1273 K with a heating rate of 0.2 K min^{-1}. And the results of both axial and radial directions were demonstrated in fig. S24.

3. Scanning Electron Microscopy (SEM) characterization and analysis

SEM images in Fig. 1B, c and fig. S14 were obtained on a Hitachi S-3500N scanning electron microscope using an accelerating voltage of 20 kV.

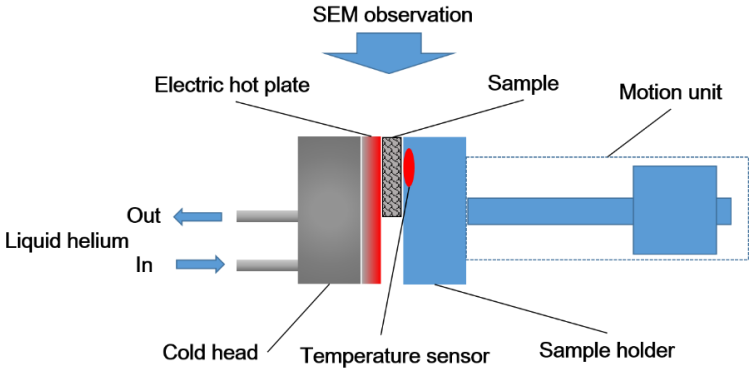

Fig. S1. The schematic of the sample platform with precise positioner and temperature control in the SEM for in situ and variable-temperature characterization. When SEM observation was performed at 4 K, the electric hot plate was set to switch off and act as thermal conductor; when SEM observation was performed at 1273 K, the refrigerant in the cold head was drained out and the electric hot plate was set to switch on.

In situ SEM images in Figs. 3 and 5A, fig. S18 and S23 and captures in Movie S3 and S4 for observing the real-time compress-release cycles at different temperatures were obtained on a ZEISS GEMINI SUPRA 55 scanning electron microscope, which was equipped with an *in situ* heating/cooling head and a micro-positioning sample holder (as shown in fig. S1), using an accelerating voltage of 10 kV and 60 μm aperture. Slices of the 3DGraphene foam were 600 μm (sample thickness, along the compression direction) × 8 mm × 5 mm for Fig. 5A and fig. S23 and Movie S3 and S4, and 500 μm × 5 mm × 5 mm for Fig. 3 and fig. S18. They were prepared by laser cutting and then manually and mechanically gripped between two counter sample holders (*i.e.*, the electric hot plate and the sample holder) without chemical binder. The holder can move with precision of 2 μm. When the SEM observation was carried out at 4 K, the electric hot plate was set to switch off and acted as thermal conductive sample holder. After about 30 minutes pre-cooling with liquid nitrogen, the cold head was then loop-filled with liquid helium (1.1 L min^{-1}) for about 50 minutes, and near 4 K temperature was achieved and detected by the temperature sensor. For SEM observation at 1273 K, the refrigerant in the cold head was drained out and the electric hot plate (tungsten, 2500 W) was set to switch on to heat the sample to 1273 K. As a result, we can perform the high temperature SEM observation subsequently after the cryogenic one for the same sample without breaking the vacuum condition, which is very important for obtaining the SEM images/captures of the same area of the same sample upon changing the temperature. A series of images for the sample were obtained successively under a set of specific conditions and then digital software VE-Viewer (Fibics Incorporated) was used to stitch the images and finish the digital position alignment. High quality SEM images and captures were conducted with ZEISS Atlas 5 system integrated with the ZEISS GEMINI SUPRA 55 scanning electron microscope.

4. Variable-temperature mechanical behaviors measurement

The stress-strain curves included results of mechanical measurements along both the axial and radial directions of the 3DGraphene foam sample from 4 K to 1273 K were obtained using a homemade mechanical analysis system which shown in fig. S2.

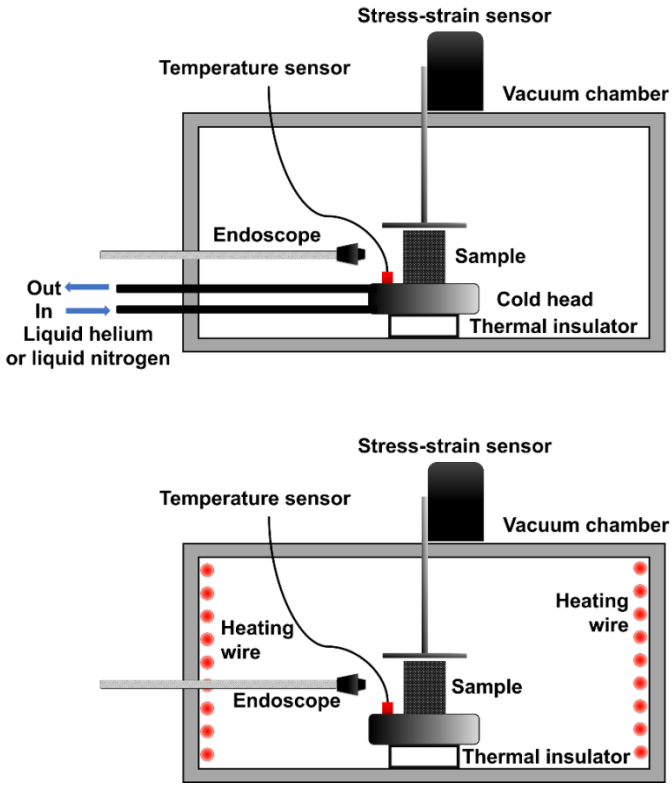

Fig. S2. Schematic of the homemade apparatus for mechanical property measurement from 4 to 1273 K. The system was mainly consisted of a vacuum chamber (both 20 cm in diameter and height) with the inner sample platform and an integrated precise positioner with 1.25 μm resolution (Model 7-PAC, SOFN Instruments CO., LTD). The stress sensor was eStrain μ-Force P4-X-O (CHIEF SI Incorporated, with 5×10^{-6} N resolution). The sample platform was connected with refrigerant pipeline for cooling down the sample. The temperature was adjusted by controlling the flow velocity of the refrigerant and measured by temperature monitor (for range from 4 K to 473 K using Lake Shore DT-670 Silicon Diode equipped with Lake Shore 211 temperature monitor in 0.15 K resolution, and for range from 673 K to 1273 K using commercial platinum rhodium thermocouple, model WRP-100, equipped with XMD-1216 temperature monitor in 0.1 K resolution, Jiangsu Plaza Premium Electric Instrument Co., Ltd.). Temperature calibration were performed before testing by setting the temperature sensor on the upper side of the sample.

Temperatures from 4 K to 43 K were obtained by using liquid helium as the refrigerant and liquid nitrogen were selected refrigerant for temperatures from 77 K to 273 K. For the temperature of 4 K, the chamber was first pre-cooling with liquid nitrogen for 30 minutes. After vacuum-pumping the liquid nitrogen out, the chamber was filled with liquid helium for 40 minutes and the cold head was also loop-filled with liquid helium (2.2 L min^{-1}). Then the helium in the chamber was sucked out and the chamber was pumped to 1.5×10^{-4} Pa. At this stage, the sample temperature was controlled and maintained at around 4 K by the liquid helium looping in the cold head. Then the tests at 4 K temperature were carried out. Then, by simply adjusting the loop rate of liquid helium in the cold head, the sample temperature could be adjusted. For example, by setting the loop rate to 1.9 L min^{-1}, the temperature was controlled at 20 K, and 1.6 L min^{-1} for 43 K. For the temperature of 77 K, the chamber was first pre-cooling with liquid nitrogen for 50 minutes, and the cold head was loop-filled with liquid nitrogen (2.6 L min^{-1}) too. Then the nitrogen in the chamber was sucked out and the chamber was pumped to 1.5×10^{-4} Pa. At this stage, the sample temperature was controlled at around 77 K. Again, by simply set the loop rate of liquid nitrogen to 1.8 L min^{-1}, the temperature was controlled at 233 K, and 1.6 L min^{-1} for 273 K.

For the measurements at the temperatures above room temperature, another configuration, an inner high temperature heater (silicon carbide heater, 4850 W power) equipped in the vacuum chamber, was used for reaching the temperature from 473 K to 1273 K. All the tests were carried out under the vacuum of 1.5×10^{-4} Pa through a molecular pump system (Edwards EXT255H). 3DGraphene foam samples (cylindrical shape, both 15 mm in diameter and height) were investigated for stress-strain characterization from 0% to 90% strain with a rate of 0.1% strain s^{-1} at 4, 20, 43, 77, 233, 273, 298, 473, 673, 873, 1073 and 1273 K, respectively (Fig. 4A). Using an endoscope, *in situ* real-time observations of the sample during the compress-release cycles at different temperatures were recorded, as shown in Movie S1 and S2 for two typical tests.

5. Young's modulus measurement

3DGraphene foam samples (cylindrical shape, both 15 mm in diameter and height) were also investigated for Young's modulus at different temperatures using the above-mentioned homemade mechanical analysis system.

(1) Standard definition: Generally, the Young's modulus is defined as the ratio of tensile or compressive stress (σ) to corresponding strain (ϵ) below the proportional limit (linear elastic range, i.e., $\sigma \propto \epsilon$) of the material (*2, 60*)

$$E = \frac{\sigma}{\epsilon} = \frac{\Delta F/A}{\Delta H/H_0} \qquad (Eq.1)$$

where $\Delta F =$ load increment, $A =$ cross-sectional area, $\Delta H =$ extension or compression increment, and $H_0 =$ initial length ($\Delta H \ll H_0$). Note that since almost all materials exhibit elastic deformation at only initial state and with small strain, this definition and their measurement of Young's modulus are only applied for the very small initial elastic strain, and are not used for large deformation materials/range.

(2) Thus, for a highly nonlinear elastic deformation (as is the case in this study), the standard definition of the Young's modulus given above could not be applied directly to measure the Young's modulus with high strains beyond the initial linear elastic range. Indeed, there are rarely study about the Young's modulus analysis with highly nonlinear elastic materials, particularly at very high strains. So, we have the definition (Eq. 2) of Young's modulus (E_ϵ) at a certain compressive strain (ϵ) of our material (with the very initial length H_0) based on the standard definition (Eq. 1) as follows: At a certain compressive strain (ϵ), a sufficient small strain (ϵ', based on the compressed length $(1-\epsilon)H_0$) induced by a stress increment ($\Delta\sigma$), could be seen as linear elastic deformation that follow the standard Young's modulus ($\Delta\sigma \propto \epsilon'$). As a result, the Young's modulus (E_ϵ) at a certain compressive strain (ϵ) can be defined as the ratio of $\Delta\sigma$ to corresponding ϵ' all over the stress-strain curve of the material in the whole testing strain range

$$E_\epsilon = \frac{\Delta\sigma}{\epsilon'} = \frac{\Delta F/A}{\Delta H/[(1-\epsilon)H_0]} \qquad (Eq.2)$$

where $\Delta F =$ load increment, $A =$ cross-sectional area, $\Delta H =$ extension or compression increment, and $H_0 =$ initial length ($\Delta H \ll (1-\epsilon)H_0$). Obviously, E_ϵ will return to the standard E at $\epsilon = 0$ (uncompressed sample with the initial linear elasticity).

(3) Test method: For practical measurements, also as demonstrated in this study (fig. S3), during stress-strain measurement, compression was interrupted by unloading-reloading cycles with a sufficient small ϵ'. With each unloading-reloading cycles the sample behaved approximately linear elasticity at each testing strain point. The Young's modulus (E_ϵ) can be calculated based on Eq. 2 with the least squares fitting data of the whole unloading-reloading process.

The detailed methods for the measurements of Young's modulus in this study are as following: during one normal measurement of stress versus strain of 3DGraphene foam, compression with rate of 0.1% engineering strain s^{-1} was interrupted (every 15% intervals in engineering strain) by unloading-reloading cycles (involving 1% true strain of the compressed sample for unloading and reloading) until a total engineering strain of 90% was reached. Young's modulus (ratio of the stress to the true strain) at each selected engineering strain (where an unloading-reloading cycle was conducted) was calculated through statistically averaging the slopes of the least squares fittings of stress versus strain during the unloading and reloading parts of the cycle, as shown in fig. S3. And such a test procedure was repeated at different temperatures along both the axial and radial directions for the Young's modulus at given temperature. All the Young's modulus were obtained following such a procedure unless otherwise explained.

In our study, we set a small ϵ' = 1% for each unloading-reloading cycle, in which the sample behaved approximately linear elasticity (inset of fig. S3) around each testing strain point. This can be seen as a special case of the general/rigorous definition of the Young's modulus at a certain compressive strain, but could be applied for the materials with high deformation range.

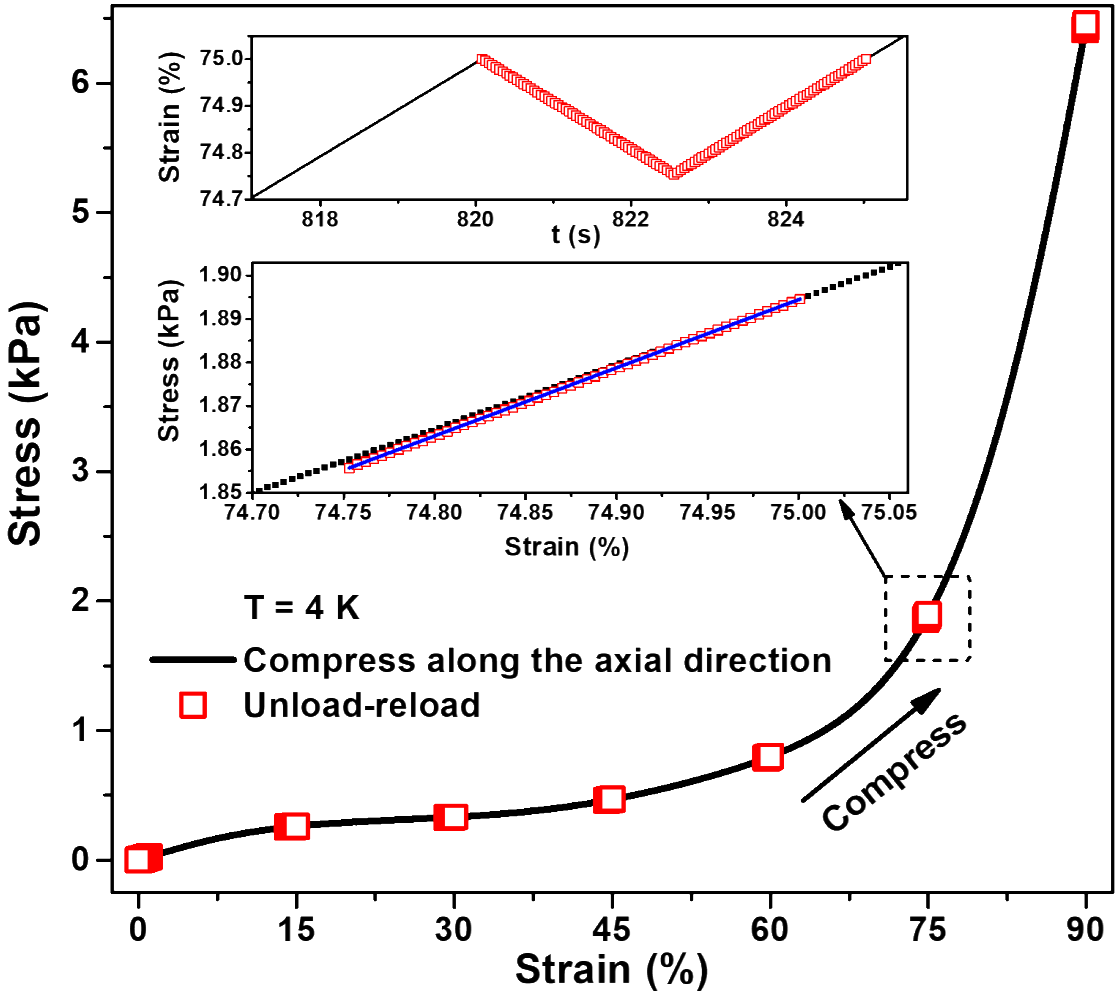

Fig. S3. Measurements of the Young's modulus of the 3DGraphene foam at 4 K. The engineering strain-time curve (top inset) and stress-engineering strain curve (bottom inset, corresponding to a 0.25% engineering strain or 1% true strain) showed details of a typical unloading-reloading cycle at 75% engineering strain. The unloading-reloading sections were highlighted using red open squares for clarity in both insets. The blue solid line in bottom inset was the least squares fitting of all the data of the whole unloading-reloading process, which was used to calculate the Young's modulus at the corresponding engineering strain by averaging the ratios of differential stress to differential true strain within the blue solid line range. Note, the Young's modulus at 0% strain was measured directly from the compress-release cycle from 0% to 1% engineering strain, and the others were measured from the unloading-reloading cycles at each 15% engineering strain intervals.

6. Poisson's ratio measurement

3DGraphene foam were cut into cubic shape (15 × 15 × 15 mm^3) using laser so that the axial direction and two orthogonal radial directions were perpendicular to the sides of the cut sample. Using endoscope and imaging processing software, the deformations required to experimentally derive the Poisson's ratios were obtained from video frames of the sample's rectangular lateral sizes during compression. The measurements provided lateral width (W) as a function of length (L) in the compression direction. Since our applied compressive strains were so large, we were in a different regime from the conventional materials that plastic deformation limited the strain range where Poisson's ratio could be obtained (*25*). However, the Poisson's ratio could still be defined using the following equation for a dynamic and large strain

$$-\mathrm{d}\log W/\mathrm{d}\log L = -(\mathrm{d}W/W)/(\mathrm{d}L/L) = \text{Poisson's Ratio}$$

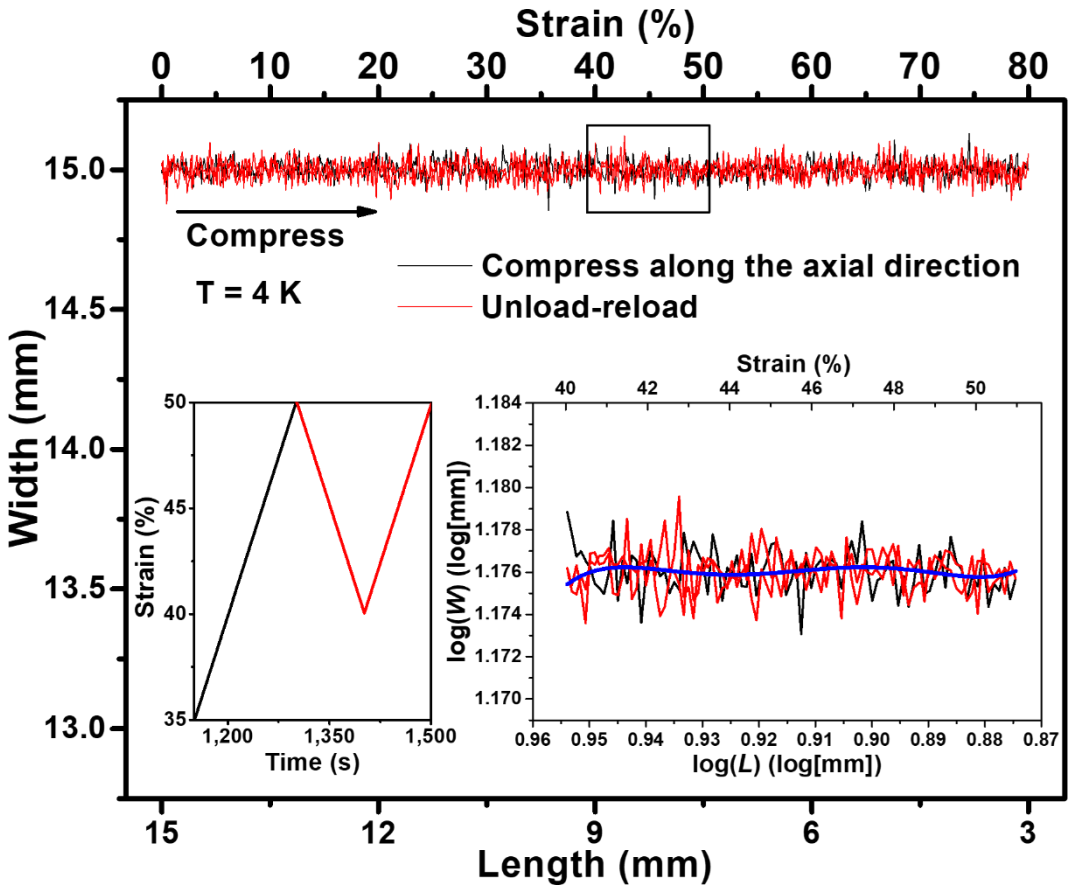

Fig. S4. Measurements of the Poisson's ratio of the 3DGraphene foam at 4 K. The left inset showed the strain-time curve of a typical unloading-reloading cycle between 40% and 50% engineering strain. The right inset was the logarithm of sample width (W) *versus* the logarithm of sample length (L) in the unloading-reloading cycle between 40% and 50% engineering strain. In both insets the unloading-reloading cycle were highlighted using red line for clarity. The blue solid curve in right inset was the least squares fitting of the reloading stage, which was used to calculate the Poisson's ratio at the corresponding engineering strain by averaging the negative slopes of log$W$ *versus* log$L$ within the blue solid line range.

So for the measurement of Poisson's ratio in our case, the sample was compressed from 0% to 80% engineering strain at a strain rate of 0.1% engineering strain s^{-1} and such process was periodically inserted by an unloading-reloading cycle (corresponding to a 10% engineering strain change also at 0.1% engineering strain s^{-1}) at each 10% engineering strain increase. Poisson's ratios were calculated through

statistically averaging the negative slopes of the least squares fittings of the log$W$ and log$L$ data in the reloading of each 10% engineering strain intervals, as shown in fig. S4. Such a test procedure was repeated at different temperatures along both the axial and radial directions. All the Poisson's ratios were obtained following such a procedure unless otherwise explained. The measurement and calculation are the same as reported earlier (*25*).

Supplementary Discussion

1. Analysis of the structural/thermal stability of chemically crosslinked nodes during the compression in wide temperature range

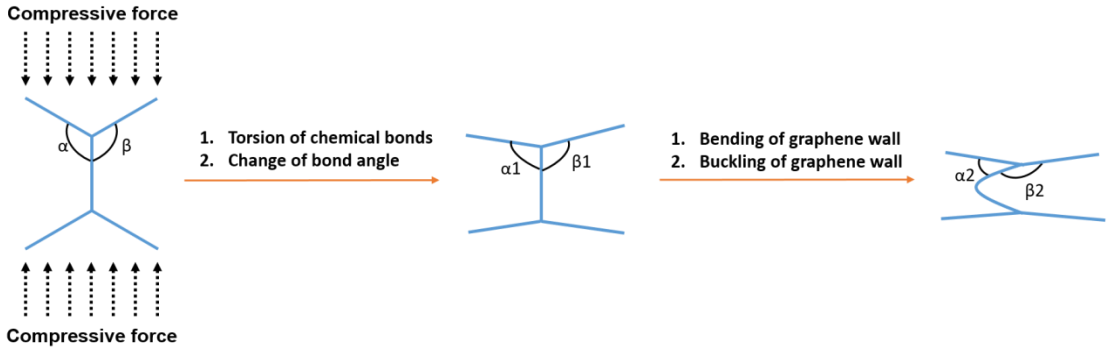

Fig. S5. The schematic of the nodes under compression.

(a) Mechanical stability:

A proposed schematic for the junction (node) between graphene sheets under compressive force was shown in fig. S5. The forces applied on the covalent bonds in the nodes that originated from compressive stress on the cell unit should include torsion force, bending force, compressive force and stretch force (*2*). Normally, torsion force, bending force and compressive force applied on the covalent bonds in the nodes could mainly result in localized chemical conformation transition (*61*) of the nodes but not destroy its structural stability unless in extreme case, which will be discussed more detailly in next section. However, once the stretch force applied on the covalent bonds in the nodes increased to be extremely large, the structure of the nodes would be unstable and the 3DGraphene foam would break up.

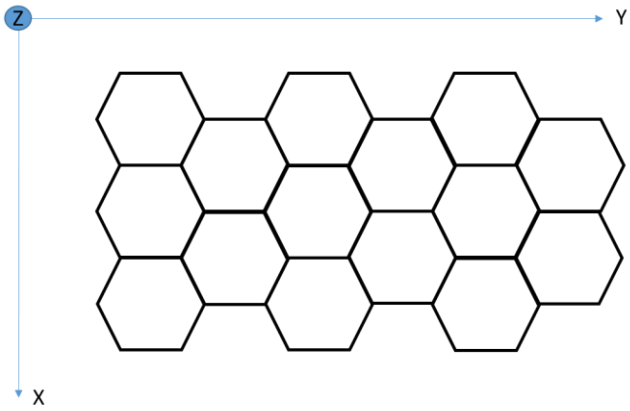

Fig. S6. The modeling architecture of the plane perpendicular to the compression direction. Considering the homogenous and isotropic structure of the 3DGraphene foam, we averaged the compressive force applied on the cross-section plane of the sample into each nodes distributed along the edges of the cell units for simple assumption, using the similar honeycomb configuration for modeling the plane which is perpendicular to the compressive direction (plane XY in fig. S6, and the compressive direction is along the Z axis direction). The stretch force on covalent bonds, as a component force of the compressive force on the nodes, were followed the same simplified processing. The total covalent bonds of the nodes in this plane should be: $N = (S/S_0) \times 2 \times (L/d_0) \times f_1 \times f_2$, in which N is the covalent bonds number, S is the area of the perpendicular plane, S_0 is the area of the hexagonal cell, 2 is the average side number of each hexagonal cell, L is the side length of the hexagonal cell, d_0 is the average distance of two edge carbon atoms along (graphene sheet) side of the hexagonal cell, f_1 is the factor describing ratio of the actual crosslinked sides to all the hexagonal cells, f_2 is the factor describing ratio of bonding atoms among all the edge carbon atoms.

For the cylindrical sample, $S = \pi r^2$, where r is the radius of the radial plane and r is 7.5 mm. And $S_0 = \frac{\sqrt{3}}{2}L^2$, where L is the side length of the hexagonal cell. Based on the SEM results (Fig. 1B, C, Fig. 3, fig. S18 and S23) and the average lateral area of the graphene oxide sheets that we used (fig. S25), we take L as 10 μm for the convenience of modeling and reasonable assumption. In addition, if all the graphene

sheets edges are zig-zag type, the d_0 should be $0.142 \times \sqrt{3} = 0.246$ nm. Due to the deviation between the open-cell cellular and randomly structure of 3DGraphene foam and the above honeycomb structure, and not all the C atoms at the edge of the graphene sheet could construct a joint covalent bond (*25*), we hypothesized f_1 and f_2 be both 0.5 for estimation and then N should be $\sim 4.2 \times 10^{11}$.

The possible covalent bonds in the chemically crosslinked nodes could be C-O, C=O, C(O)-O, C-C and C=C (*25, 35, 36*). Generally double bond is stronger than single bond, and the typical rupture force of single covalent bond (C-C and C-O) under stretching should be at 4.0~4.5 nN (*62*). So all the covalent bonds at nodes in the model plane could undertake rupture force at least $\sim 1.8 \times 10^3$ N. The compressive force applied on the sample at the large strain (90%) should be σS, where σ is the corresponding stress and S is the cross-section area of the sample along the radial direction, and then this force should be ~1.2 N (7 kPa × 3.14 × 0.0075^2 m^2). Therefore, the real average stretch force applied on the covalent bonds (component force of the compressive force on the nodes) should be several orders smaller than the force it could withstand. While in general the mechanical rupture happens first at the weakest point, it would be very unlikely the applied force could be concentrated on a few joint bonds at the molecular level for the nearly homogeneous and isotropic material in this case. Conclusively, the chemically crosslinked nodes will be stable even at large strain (*3*). The key point for such overall structure integrity stability is also due to the large void space between the chemically crosslinked graphene sheets, which offers the cushion room, different from the conventional materials.

(b) Thermal stability:

The discussion above is for the situation at the room temperature (T = 298 K). The rupture force of single covalent bond at temperature near absolutely zero is slightly larger than (or nearly the same with) the force at room temperature (*63*), so the stability of the chemically crosslinked nodes at cryogenic temperature of 4 K for our situation should be kept. Theoretically, the rupture force of the covalent bond should decrease with the increasing temperature (*64*). Though the specific values of the

rupture force of covalent bond under high temperature (such as 1273 K) is unclear, there would not be order of magnitudes change just from 298 to 1273 K based on the original function ($v \sim \omega_0 \exp[(E_b - f x_0)/k_b T]$, where f is the rupture force) (*8*). Therefore, we believe that chemically crosslinked nodes and the overall structural integrity of the 3DGraphene foam will not be damaged at 1273 K. This is also proved experimentally by our works (Movie S2 and S4) (*1*) and the literature which proved that above-mentioned covalent bonds are stable below 1800 °C (*65*).

Generally, it is believed that bonds such as C=C/C-C/C-O are thermally stable due to their high bonding energy (~145/80/86 Kcal/mol). Considering the large conjugation system of this material (mainly as large aromatic system such as graphene sheets), the thermal stability should be further enhanced. In our case, annealing during high temperature tests should remove significant O containing groups as supported by decreased O amount (*25, 36*). Nevertheless, there are still some C-O/C=O remains after high temperature annealing (*25, 35, 36*). It is well known that even after over 2000 °C annealing during carbon fiber preparation, there is still some O left (normally 0.1-0.3%) in fiber in the form of O containing groups (*65, 66*). Importantly, cross-links between neighboring graphene sheets via oxygen functional cross-links may also be created up on thermal annealing (*65*). These results indicate that the covalent bonding nature at the junction sites would not be changed under high temperature conditions. As indicated by the repeating test results (the well-kept properties after 100-times testing at high temperatures shown in fig. S21 and S29, and the well-kept elastic deformation at 1273 K shown in Movie S2 and S4), it is believed the material (graphene sheets and covalent bonds) is rather stable, though it cannot be ruled out completely that some very minor/slow reaction could happen at high temperature for rather slow degradation due to the possible reaction between O and C atoms (groups).

Note, above discussions are based on a periodic model and simple estimation. In fact, local stress concentration could happen in some nodes and involving covalent bonds could fail under localized large stretching force. However, such failure should be rare

as mentioned above due to the nearly homogeneous and isotropic materials in this case.

2. Simulation of compressive deformation mechanism and analysis of the temperature dependence

In the whole compression process, as shown in Fig. 2B (and 4A), the 3DGraphene foam demonstrated a short linear-elastic regime following by a plateau of roughly constant stress, and finally leading into the regime of steeply rising stress. Each regime could probably associate with one or several dominated mechanisms of deformation, and *in situ* photographing (Figs. 3 and 5A, fig. S18 and S23, and Movie S3 and S4) of the material in the loading/deformation process combined with the theoretical deformation analysis/simulation made such identification be possible.

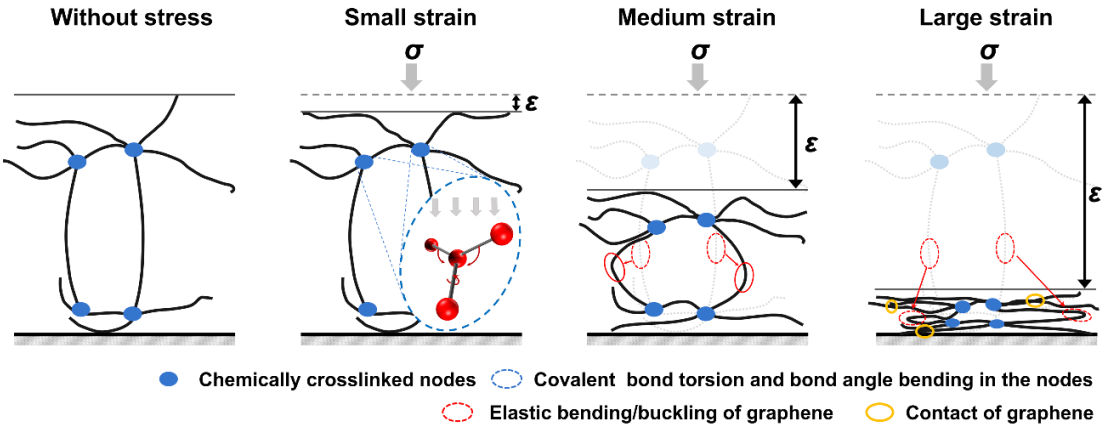

Fig. S7. Schematic of the proposed elastic deformation of the 3DGraphene foam under compressive stress. The chemically crosslinked nodes keep structural integrity with localized conformation adjustment through covalent bond torsion and bond angle bending, combined with the subsequent elastic bending and/or buckling of the graphene sheets.

Here, as shown in fig. S7, we envisage that once the compressive stress loading on the material, the torsion deformation of the covalent bonds (the dihedral angle torsion) and the bond angle bending (*46*), which mostly should locate and occur at the nodes (*67*), should appear immediately because of the easily understandable small energy/force demands of these deformation modes. Localized elastic bending of the

graphene walls could probably appear too (as shown in Figs 3 and 5A and fig. S18 and S23), and all these modes should give the linear elasticity region in the stress-strain curve of the material (*68*). Then, the elastic bending of the graphene walls should develop further with increasing compressive strain of the sample (Figs. 3 and 5A and fig. S18 and S23). Moreover, when a critical stress was reached, a certain portion of the cell walls that satisfy the critical condition began to collapse by the elastic buckling (which should be elastically recoverable) (*39*). The integrated stress of these two deformation modes should exhibit an approximate plateau with gentle increase. Eventually, at high strains of the sample, the cell collapsed and deformed sufficiently that some cell walls touched each other, and some graphene walls would bend more seriously with quite large curvature under increasing compressive deformation of the sample. The highly compressed material should combine different kinds of highly developed deformation modes and the spatial density of all these deformation points should increase quickly under large strain of the sample too, which would result in the final steeply rising portion of the stress-strain curve that named densification (*2, 69*). In addition, the 3DGraphene foam possesses a porosity of ~99.93%. Such large cushion space (voids) between the cell walls enable sufficient freedom not only for large deformations during loading but also for efficient recovery of the cell walls upon unloading.

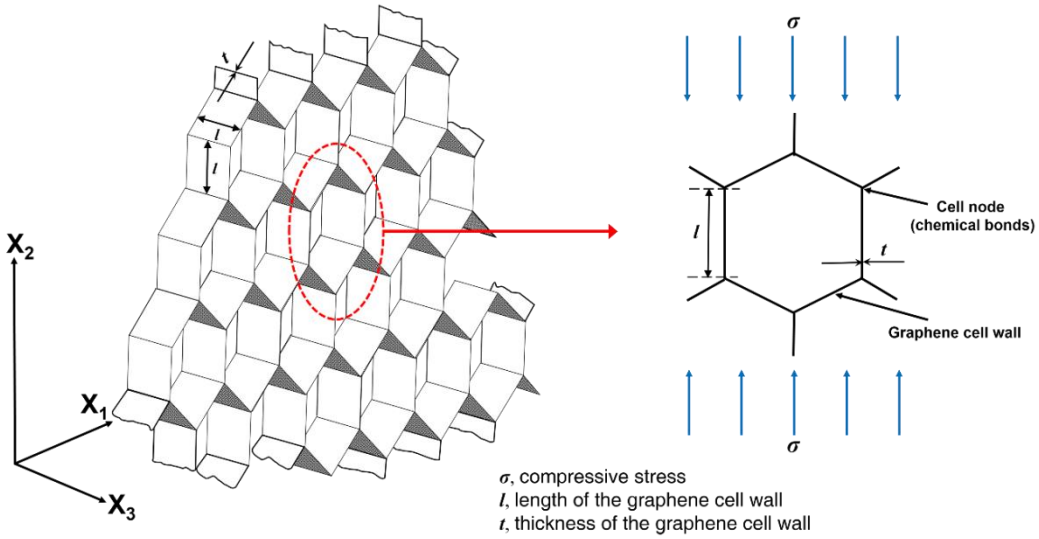

Fig. S8. The schematic of the periodic honeycomb-like cell architecture for modeling the 3DGraphene foam and enlargement of one unit cell under the applied compressive stress. Generally, the properties of the foam/cellular material are not only determined by the intrinsic properties of the building blocks, but also in terms of its structure (*2*). Because of the complex and random structure of the 3DGraphene foam, we model the compressive deformation roughly based on a simple and periodic honeycomb-like cell architecture (fig. S8) for the simulation, where three single layer graphene sheets (cell walls) are jointed/connected together in nodes along their edges *via* covalent bonds and only in-plane (plane X_1X_2) deformation is taken into consideration (because of the near-zero Poisson's ratio, the deformation of the cell unit along the X_1X_3 plane which was perpendicular to the compressed direction, should be negligible here). Based on our previous works (*25*, *35*, *36*) and our understanding of the 3DGraphene foam, the covalent bonds in the nodes could be C-O, C=O, C(O)-O, C-C and C=C, or a combination of them. Considering their relatively small difference of bond strength in theory, and the dominated portion of the C-O bonds, we consider only C-O bonds for an easy estimation.

As discussed above, the compressive deformation of the structure could be simulated through the combination of several potential modes: elastic torsion of the covalent bonds (the torsion of the dihedral angel), bending of the bond angle, elastic bending of the graphene walls, elastic buckling of the graphene walls, local compression/bending

of the graphene in the densification stage. Based on the theory of modified continuum mechanics (*70*), these modes can be defined respectively as follows:

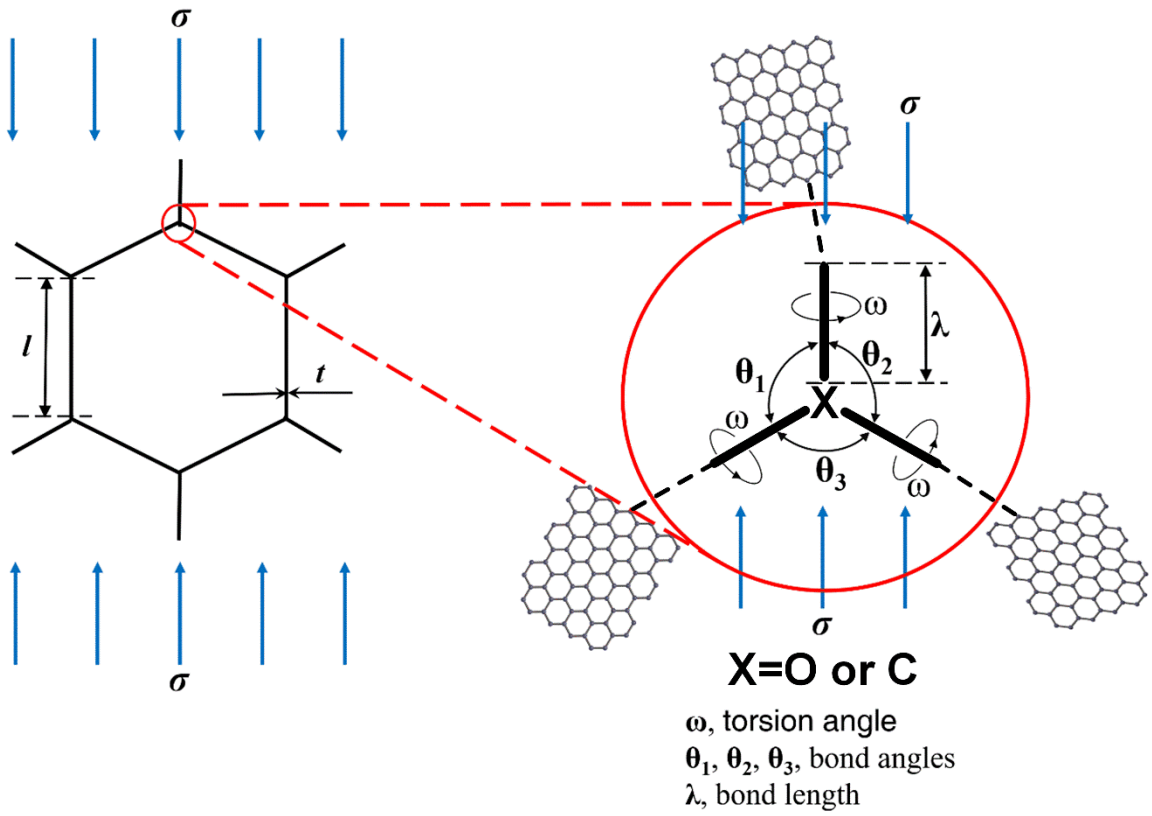

Fig. S9. The schematic of a cell node under the applied compressive stress.

(1) Elastic torsion of the covalent bonds as shown in fig. S9.

The torsional energy E_τ can be represented as following (*71*)

$$E_\tau = (V_1/2)(1+\cos\omega) + (V_2/2)(1-\cos 2\omega) + (V_3/2)(1+\cos 3\omega)$$

where V_1, V_2, and V_3 are the torsion parameters of the covalent bond, and ω is the torsion angle.

(2) Elastic bending of the covalent bond angles as shown in fig. S9.

The bending energy of elastic bending of the bond angle E_θ can be approximated in terms of elastic springs as following (*72*)

$$E_\theta = \frac{1}{2} k_\theta (\theta' - \theta^0)^2$$

where k_θ is the angle bending force constant, θ^0 and θ' are bond angles before and after the bending.

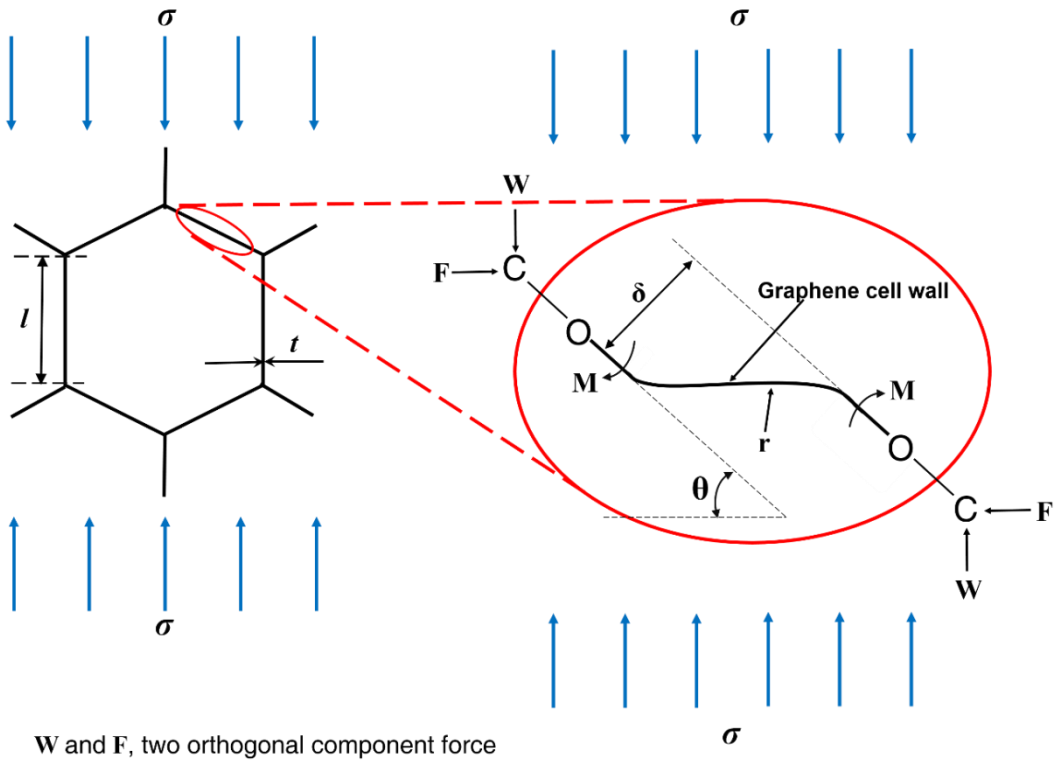

Fig. S10. The schematic of elastic bending of the graphene cell wall under the applied compressive stress. θ_3 is the same angle in fig. S9.

(3) Elastic bending of the graphene at small strain of the sample as shown in fig. S10. At small strains of the sample, the graphene sheets individually subject to bending to a certain curvature. As reported elsewhere (*53*, *73*), the energy of elastic bending of the graphene, E_{bending}, can be represented as following

$$E_{\text{bending}} = \frac{1}{2} N S_0 B_{\text{M}} r^{-2}$$

where N is the number of atoms within the graphene sheet, S_0 is the average area of carbon atom, B_{M} is the bending rigidity of graphene, and r is the bending radius.

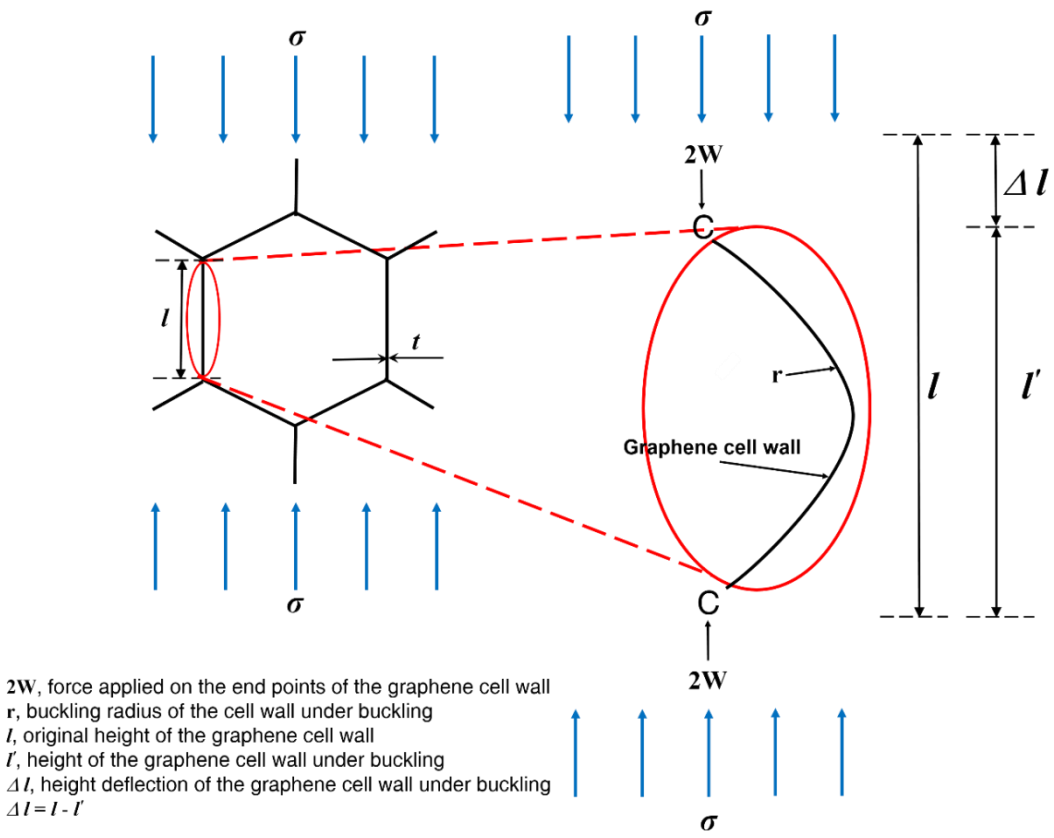

Fig. S11. The schematic of elastic buckling of the graphene cell wall under the applied compressive stress. (4) Elastic buckling of the graphene as shown in fig. S11.

Here, we analyze the buckling of graphene cell wall based on the continuum mechanics (*41*), where the related energy of potential elastic buckling of graphene struts, E_{buckling}, can be obtained by following integral equation

$$E_{\text{buckling}} = \int \frac{1}{2} N S_0 B_{\text{M}} r^{-2}$$

where N is the number of atoms within the graphene sheet, S_0 is the average area of carbon atom, B_{M} is the bending rigidity of graphene, and r is the curvature radius along the buckled graphene sheet/cell wall. The integration is taken along the deflection curve under buckling.

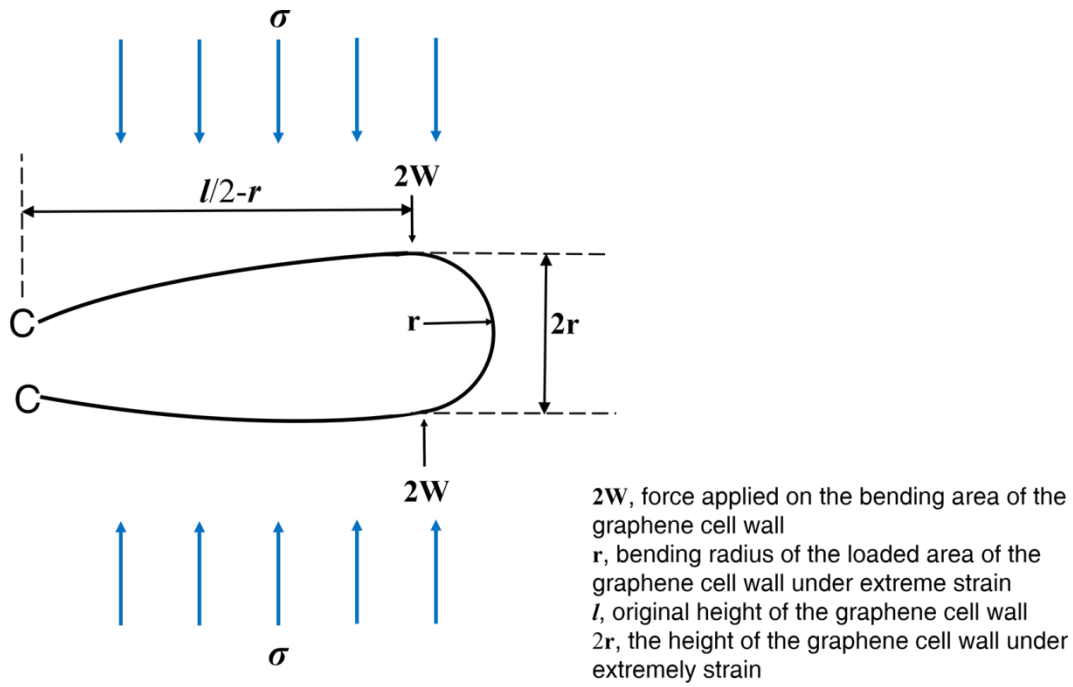

Fig. S12. The schematic of deeply elastic bending of the graphene cell wall at large strain of the sample. (5) Elastic bending of the graphene at large strain of the sample as shown in fig. S12.

At large strain of the sample, a certain portion of graphene sheets are supposed to be nearly folded and even squeeze each other and the graphene sheet is deeply compressed to a very small radius at the sharp bending area. So the related energy can be expressed as the similar formula in above mode 3 (*53*, *54*)

$$E_{\text{bending,large}} = \frac{1}{2} N_{\text{l}} S_0 B_{\text{M}} r^{-2}$$

where N_{l} varied from N in equation of mode 3 is the number of atoms within the specific bending area, S_0 is the average area of carbon atom, B_{M} is the bending rigidity of graphene, and r is the bending radius.

With all these modes combined, so totally, the energy of one cell in the honeycomb-like cell architecture, E_{total}, should be the sum of energies of the supposed modes as following

$$E_{\text{total}} = C_1[(V_1/2)(1+\cos\omega) + (V_2/2)(1-\cos 2\omega) + (V_3/2)(1+\cos 3\omega)] + C_2\left[\frac{1}{2}k_{\theta 1}\Delta\theta_1{}^2 + \frac{1}{2}k_{\theta 2}\Delta\theta_2{}^2 + \frac{1}{2}k_{\theta 3}\Delta\theta_3{}^2\right] + C_3\frac{1}{2}NS_0B_{\text{M}}r^{-2} + C_4\int\frac{1}{2}NS_0B_{\text{M}}r^{-2}$$

where C_1, C_2, C_3, C_4 are constant parameters that represent the weight coefficient of each mode taken into calculation, and θ_1, θ_2 and θ_3 are three bond angles in each node as shown in fig. S9.

Using $P = \mathrm{d}E/\mathrm{d}x$, $\sigma = P/\Omega$, and $\varepsilon = \mathrm{d}x/x_0$, we can derive

$$\sigma = \frac{1}{2(\mathrm{l}+\lambda)^3\sin\frac{\theta_3}{2}\left(1+\cos\frac{\theta_3}{2}\right)}\frac{\mathrm{d}E}{\varepsilon}$$

where P is the compressive force applied on the cell, $\mathrm{d}E$ is the differential of energy, x is the height of the unit cell under P, σ is the stress applied on the cell corresponding to P, $\Omega = 2(\mathrm{l}+\lambda)^2\sin(\theta_3/2)$ is the area that P applied on, ε is the strain of the cell under σ, $\mathrm{d}x$ is the height deflection of the cell under σ, and $x_0 = (\mathrm{l}+\lambda)[1+\cos(\theta_3/2)]$ is the original height of the cell, and λ is C-O bond length. Note the stress and strain of a unit cell are equal to the stress and strain of the whole structure for uniform regular structure based on periodic unit cells.

Since

$$\mathrm{d}E = \mathrm{d}E_{\text{total}} = C_1[(V_1/2)(-\sin\omega)\mathrm{d}\omega + (V_2/2)(2\sin 2\omega)\mathrm{d}\omega + (V_3/2)(-3\sin 3\omega)\mathrm{d}\omega] + C_2[k_{\theta 1}\mathrm{d}\theta_1 + k_{\theta 2}\mathrm{d}\theta_2 + k_{\theta 3}\mathrm{d}\theta_3] - C_3NS_0B_{\text{M}}r^{-3}\mathrm{d}r - C_4\mathrm{d}r\int NS_0B_{\text{M}}r^{-3}$$

And

$$\varepsilon_\omega = \frac{\mathrm{d}\omega}{2\pi}\mathrm{d}x$$

which is the strain of the cell corresponding to torsion deformation of the covalent bond.

Also, $\theta_1 = \theta_2 = \pi - \frac{\theta_3}{2}$, and $\varepsilon_{\theta_3} = \frac{\mathrm{d}\theta_3}{\cos\frac{\theta_3}{2}}$ which is the strain of the cell corresponding to the bending of bond angle θ_3 (which was simplified as O-C-O bond angle), and

$$\varepsilon_{\mathrm{bend,small}} = \frac{\delta \sin\theta}{(\mathrm{l}+\lambda)\cos\theta}$$

which is the strain of the cell corresponding to bending of the graphene cell wall at small strain of the sample, where δ is the graphene cell wall deflection, and θ is a structural parameter, both are defined in fig. S9. From the standard beam theory (*2*) the wall deflects by

$$\delta = M \cdot \frac{(\mathrm{l}+\lambda)^2}{6B_{\mathrm{M}}}$$

where the bending moment $M = \frac{W(\mathrm{l}+\lambda)\cos\theta}{2}$, and at equilibrium the component force (as shown in fig. S10) $F = 0$ and $W = \sigma(\mathrm{l}+\lambda)^2\cos\theta$. Then

$$\varepsilon_{\mathrm{buckle}} = \frac{2}{\mathrm{l}+\lambda}\left[\mathrm{d}r \cdot \sin\frac{\mathrm{l}+\lambda}{2r} + r \cdot d\left(\sin\frac{\mathrm{l}+r}{2r}\right)\right]$$

which is the strain of the cell corresponding to buckling of the graphene cell wall, and

$$\varepsilon_{\mathrm{bend,large}} = \frac{\mathrm{d}r}{r}$$

which is the strain of the cell corresponding to bending of the graphene cell wall at large strain of the sample.

Note $\varepsilon = \varepsilon_{\omega} + \varepsilon_{\theta 3} + \varepsilon_{\mathrm{bend,small}} + \varepsilon_{\mathrm{buckle}} + \varepsilon_{\mathrm{bend,large}}$, so all the calculation above giving

$$\sigma = C_1 A_\tau \varepsilon + C_2 B_\theta \varepsilon + C_{3,1} C_{\text{bend,small}} \varepsilon + C_4 D_{\text{buckle}} \left[-\frac{1}{2}\varepsilon^2 + \frac{1}{3}\varepsilon^3 + \cdots + (-1)^n \frac{\varepsilon^{n+1}}{n+1} + \cdots \right] + C_{3,2} C_{\text{bend,large}} \frac{1}{\sqrt{2}\pi^2} \left(\frac{\varepsilon}{1-\varepsilon} \right)^2$$

Using fifth order approximation for strain ε, one can derive the following stress-strain relationship

$$\sigma = \left(C_1 A_\tau + C_2 B_\theta + C_{3,1} C_{\text{bend,small}} \right) \varepsilon + C_4 D_{\text{buckle}} \left[-\frac{1}{2}\varepsilon^2 + \frac{1}{3}\varepsilon^3 - \frac{1}{4}\varepsilon^4 + \frac{1}{5}\varepsilon^5 \right] + C_{3,2} C_{\text{bend,large}} \frac{\sqrt{3}}{2\pi} \varepsilon^5$$

where $C_{3,1}$, $C_{3,2}$ are constant parameters that represent the weight coefficient of elastic bending at small and large strain of the sample, and A_τ, B_θ, $C_{\text{bend,small}}$, D_{buckle}, and $C_{\text{bend,large}}$ are calculated parameters that corresponding to covalent bond torsion, bond angle bending, graphene bending at small strain of the sample, graphene buckling and graphene bending at large strain of the sample, respectively, which are listed as follow

$$A_\tau = \frac{\sqrt{3}}{2} \pi \frac{V_n}{\lambda^3}$$

$$B_\theta = -\cos\theta_3 \frac{2}{\lambda^2 t} k_\theta$$

$$C_{\text{bend,small}} = \frac{3 B_M}{l t^3}$$

$$D_{\text{buckle}} = \frac{\pi}{4} \frac{B_M}{l t^3}$$

$$C_{\text{bend,large}} = \frac{2\pi B_M}{l t^3}$$

where λ is the length of the covalent bonds, t is the thickness of the graphene cell wall (the thickness of the beam).

Obviously, the obtained stress-strain relationship above possesses a high order polynomial form, which corresponds to the experimentally observed nonlinear elasticity as reported elsewhere (*54*). Importantly, the obtained stress-strain relationship above indeed reflect and agree with the observed temperature-invariant mechanical properties of individual graphene sheets, junction sites and the bulk material, in terms of the calculation parameters (A_τ, B_θ, $C_{\mathrm{bend,small}}$, D_{buckle}, and $C_{\mathrm{bend,large}}$) related to the intrinsic and temperature-invariant mechanical properties of individual graphene sheets, junction sites. In contrast, no such high elasticity and temperature-invariant properties exhibited by our material could be obtained by applying the same model (with 5th or higher order) for traditional foam materials and use the properties of their cell walls and junctions (such as commercial polyurethane foam) (*2*). As a result, to investigate the temperature dependence of the mechanical properties of the 3DGraphene foam in the compression, the temperature influence of above mentioned deformation modes and corresponding parameters should be taken into account and discussed as following.

Here, the covalent bond torsion parameter $V_n = V_1 = V_2 = V_3 = 2 \times \frac{1.15}{4}$ kcal mol^{-1} (*51, 52, 74*) is temperature-invariant ($K_{IJKL}^T = K_{IJKL}^0$, where T is the temperature) (*30, 75, 76*); θ_3 has a value set to be in the range of 100~120° (considering the core atom of the bond angle should be C or O, for which sp^3 and sp^2 hybridization are the dominated form) and independent of the temperature (*77*); for the majority of models used, the thickness of single layer graphene t = 0.34 nm, which is also assumed to be independent of the temperature, since the nature of only one atomic thickness; the cell wall length l is set to be 10 μm as discussed in above section, which does not change at different temperature.

Next, the covalent bond length depends on temperature *via* $\lambda = \lambda_0(1+\alpha T)$ (*48*), in which T is the absolute temperature, α is the thermal expansion coefficient of the C-O bond. As shown in fig. S24, the 3DGraphene foam exhibited very small thermal expansion coefficient at ~3 × 10^{-6} K^{-1}. There should be two factors contributing to the material's thermal expansion, the graphene cell walls and the cell nodes. As it has

been reported that graphene sheet possesses a thermal expansion coefficient in the order of 10^{-6} K^{-1} too (*78*), it can be assumed that the thermal expansion coefficient of the covalent bond in the nodes is no larger than the order of 10^{-6} K^{-1}. Even taken 9 × 10^{-6} K^{-1} into calculation, the force constant K_q exhibits only a variance of 0.009 at most in our investigated temperature range of 10^3 K, thus it has very small influence on the final result. On the other hand, from the structural and chemical viewpoints, C-O and C-C bonds are very similar, so the thermal expansion coefficient of them should not have large difference either (about 1~2 × 10^{-6} $K^{-1}$for C-C bond). With all these in mind, we take 3.0 × 10^{-6} K^{-1} as the estimated value for thermal expansion coefficient of the C-O bond.

Also, λ_0 = 140~145 pm is the C-O bond length at T = 298 K (*77*, *79*).

The covalent bond angle bending force constant depends on temperature *via*

$$k_\theta = \frac{\beta Z_O^* Z_C^*}{\{[2\lambda_0^2(1+\alpha T)^2](1-\cos\theta_3)\}^{5/2}} \times {\lambda_0}^4(1+\alpha T)^4(3\sin{\theta_3}^2 - \cos\theta_3)$$

where $\beta = \frac{664.12}{\lambda_0^2(1+\alpha T)^2}$, $Z_O^* = 2.3$ and $Z_C^* = 1.912$ are effective charges of O and C atom respectively.

The bending rigidity of graphene depends on temperature *via* (*47*, *73*)

$$B_M = 1.12\exp(-8.1k_B T)$$

where k_B is the Boltzmann constant.

Based on these, we can calculate that at room temperature (T = 298 K), A_τ = 1.23~1.28×10^{-6} kPa, B_θ = 2.3~5.6×10^{-5} kPa, $C_{bend,\ small}$ = 1.76 kPa, D_{buckle} = 4.6 kPa, $C_{bend,\ large}$ = 3.68 kPa.

Considering the complexity/disorder of the actual foam structure, we have made some modification to improve the accuracy of the model. Here, some factors should be considered to determine the weight coefficient parameters of each deformations

modes: (1) not all the C atoms at the edge of the graphene sheet could construct an joint covalent bond (C-O bond); (2) because of the deviation between the three-dimensional open-cell structure of 3DGraphene foam and above honeycomb-like cell structure which considering deformation only in one plane paralleled to the compressive stress, just part of the graphene sheets should be involved to calculate; (3) the actual graphene sheets in the material are not ideal square, so only part of the graphene sheet edges should be involved; (4) not all the crosslinked sites in the nodes have connectivity of three, which means the number of the bending bond angles should be decreased; (5) elastic bending of the graphene sheets probably be more frequent than elastic buckling of the graphene sheets. With all these as guidance and iterative optimization, the simulated stress-strain curve of the 3DGraphene foam under 298 K agreed well with the experimental result by setting C_1 as 0.24, C_2 as 0.13, $C_{3,1}$ as 0.7, C_4 as 0.14 and $C_{3,2}$ as 0.9, as shown in fig. S26. In addition, the graphene cell walls should possess even an amount of defects (*80*). However, based on the *in situ* SEM observation (Fig. 3 and 5A, fig. S18 and S23, Movie S3 and S4), there were no cell wall fracture and structural damage observed, indicating the high mechanical stability of the graphene cell walls even with existence of defects. First of all, the graphene sheets intrinsically possess ultra-high in-plane strength with very high energy for defect formation (*26, 34*). Moreover, the nearly homogeneous and isotropic structure endues efficient load transfer and prevent local stress concentration in some localized defects (*2, 14*). Also, the large cushion space between the graphene cell walls could accommodate the possible local stress concentration and prevent further defect formation (*14*).

The formula about the temperature influence of stress (σ) at a given strain (ε) could be deduced from above equations as following, which could clearly exhibit the temperature dependency of mechanical properties of 3DGraphene foam

$$\sigma = \left\{ \frac{C_1 A_\tau^{298\mathrm{K}}}{[1+\alpha(T-298)]^3} + \frac{C_2 B_\theta^{298\mathrm{K}}}{[1+\alpha(T-298)]^5} + C_{3,1}\left[C_{\mathrm{bend,small}}^{298\mathrm{K}} - \frac{3\mu k_\mathrm{B}(T-298)}{lt^3} \right] \right\} \varepsilon + C_4 \left[D_{\mathrm{buckle}}^{298\mathrm{K}} - \frac{\pi\mu k_\mathrm{B}(T-298)}{4lt^3} \right] \left[-\frac{1}{2}\varepsilon^2 + \frac{1}{3}\varepsilon^3 - \frac{1}{4}\varepsilon^4 + \frac{1}{5}\varepsilon^5 \right] + C_{3,2}\left[\mathrm{C}_{\mathrm{bend,large}}^{298\mathrm{K}} - \frac{2\pi\mu k_\mathrm{B}(T-298)}{lt^3} \right] \cdot \frac{\sqrt{3}}{2\pi}\varepsilon^5$$

Here, we set C_1, C_2, $C_{3,1}$, C_4 and $C_{3,2}$ be the same value as those at 298 K. $A_\tau^{298\mathrm{K}}$, $B_\theta^{298\mathrm{K}}$, $C_{\mathrm{bend,small}}^{298\mathrm{K}}$, $D_{\mathrm{buckle}}^{298\mathrm{K}}$ and $C_{\mathrm{bend,large}}^{298\mathrm{K}}$ are those parameters at T = 298 K, and μ = 9.07 is the fitting parameter, a dimensionless parameter which depends on the system size and a characteristic length (*47*). With these, the simulated stress-strain curves at 4 K (Fig. 5B) and 1273 K (Fig. 5C) also showed great agreement with the experimental data. Then we used this formula to derive the stress (σ) dependence on temperature (T) at fixed strains of ε = 6%, 40% and 80%, respectively. The results were shown in Fig. 5D, and the experimental data agreed very well with the calculated curves, which showed a very small temperature dependence of the stress in the investigated temperature range down to deep cryogenic temperature (4 K). The results demonstrated clearly that the origins of the temperature-invariant properties of 3DGraphene foam are the quite small temperature influence on the mechanical properties of chemically crosslinked nodes (covalent bonds) and the graphene sheets (cell walls) from 4 K to 1273 K.

As shown in bottom inset of fig. S3, the stress-strain curve of the unloading-reloading cycle (red open squares) showed indiscernible hysteresis and almost completely coincided with the original stress-strain curve (black solid squares). Such negligible difference should be the results of: (1) the special mechanical properties of 3DGraphene foam which from the unique intrinsic properties of graphene sheets and structure of the 3DGraphene foam; (2) the very slow strain rate applied on the sample

in this measurement; (3) the vacuum environment excludes the disturbance from the interaction between the 3DGraphene foam and the fluid such as air; (4) the super compressive elasticity of 3DGraphene foam in large strain range made each small enough strain range with small enough strain rate be nearly linearly elastic. So based on above definition of Young's modulus, we could obtain an approximate Young's modulus-engineering strain curve using the stress value of the normal stress-strain curve with quasi-static strain rate but not that from an designed and inserted unloading-reloading cycle (certainly the strain should be true strain considering the definition of Young's modulus). The results were shown in fig. S27, which exhibited similar values but larger standard deviations compared with those from our standard method for Young's modulus (obtained from inserted unloading-reloading cycle) at the same engineering strain.

Similarly, now that we can obtain the theoretically simulated stress-strain curve as shown in Fig. 5B, C, and fig. S26, using the definition of Young's modulus and discussion above, the Young's modulus (*E*) should be approximately simulated by

$$E = \frac{\mathrm{d}\sigma}{\mathrm{d}\varepsilon'} = \frac{\mathrm{d}\sigma}{\mathrm{d}[ln(1+\varepsilon)]} = \frac{\mathrm{d}\sigma}{\frac{1}{1+\varepsilon}\mathrm{d}\varepsilon}$$

$$= \left(C_1 A_\tau + C_2 B_\theta + C_{3,1} C_{\mathrm{bend,small}}\right)(1+\varepsilon)$$

$$+ C_4 D_{\mathrm{buckle}}[-\varepsilon + \varepsilon^2 - \varepsilon^3 + \varepsilon^4](1+\varepsilon) + C_{3,2} C_{\mathrm{bend,large}} \frac{5\sqrt{3}}{2\pi} \varepsilon^4 (1 + \varepsilon)$$

where the ε' is the ture strain and ε is the engineering strain, and $\varepsilon' = \ln(1+\varepsilon)$ (*2*).

Moreover, the temperature influence of Young's modulus (*E*) should approximately be

$$E = \frac{\mathrm{d}\sigma}{\mathrm{d}\varepsilon'} = \left\{ \frac{C_1 A_\tau^{298\mathrm{K}}}{[1+\alpha(T-298)]^3} + \frac{C_2 B_\theta^{298\mathrm{K}}}{[1+\alpha(T-298)]^5} \right.$$

$$\left. + C_{3,1}\left[C_{\mathrm{bend,small}}^{298\mathrm{K}} - \frac{3\mu k_\mathrm{B}(T-298)}{lt^3} \right] \right\}(1+\varepsilon)$$

$$+ C_4\left[D_{\mathrm{buckle}}^{298\mathrm{K}} - \frac{\pi\mu k_\mathrm{B}(T-298)}{4lt^3} \right][-\varepsilon+\varepsilon^2-\varepsilon^3+\varepsilon^4](1+\varepsilon)$$

$$+ C_{3,2}\left[C_{\mathrm{bend,large}}^{298\mathrm{K}} - \frac{2\pi\mu k_\mathrm{B}(T-298)}{lt^3} \right] \cdot \frac{5\sqrt{3}}{2\pi}\varepsilon^4(1+\varepsilon)$$

Above simulation results were plotted as the Fig. 5E, insets of Fig. 5B, C, and inset of fig. S26, which all matched well with the experimental results from the standard method for Young's modulus measurement (and experimental results from the normal stress-strain curves). These not only demonstrated clearly the same origins of the temperature-invariance of Young's modulus down to deep cryogenic temperature of 4 K, but also proved the rationality of both our whole simulation and the approximate method for obtaining Young's modulus using the normal stress-strain curve.

Similarly, we could obtain the tangent modulus (ratio of the stress to the engineering strain) of 3DGraphene foam by calculating the slopes at each strain of the stress-strain curve that could be the normal experimental one or the theoretically simulated one. The two curves matched quite well as shown in fig. S28.

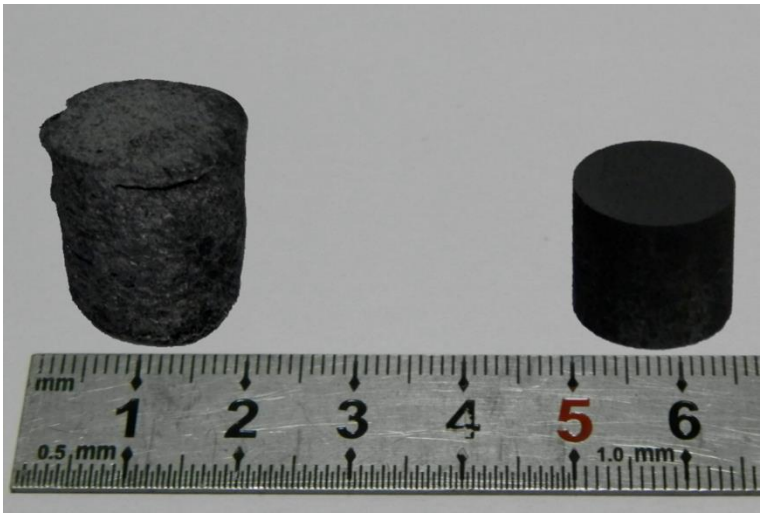

Fig. S13. The photograph of the 3DGraphene foam samples. The as-prepared one with somewhat irregular surface (left) and the laser cut one with pretty cylinder shape of both 15 mm in diameter and height (right).

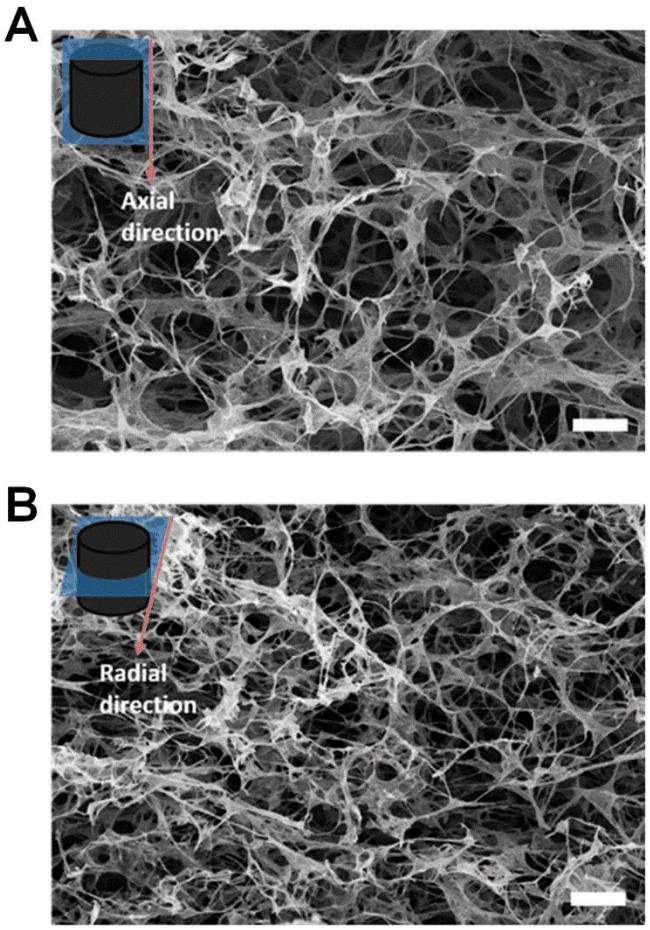

Fig. S14. Cross-sectional SEM images of the 3DGraphene foam. (**A**) Cross-section along the axial direction**.** (**B**) Cross-section along the radial direction. The material demonstrated isotropic morphology at both directions, ensuring isotropic mechanical properties. The scale bars were both 50 μm.

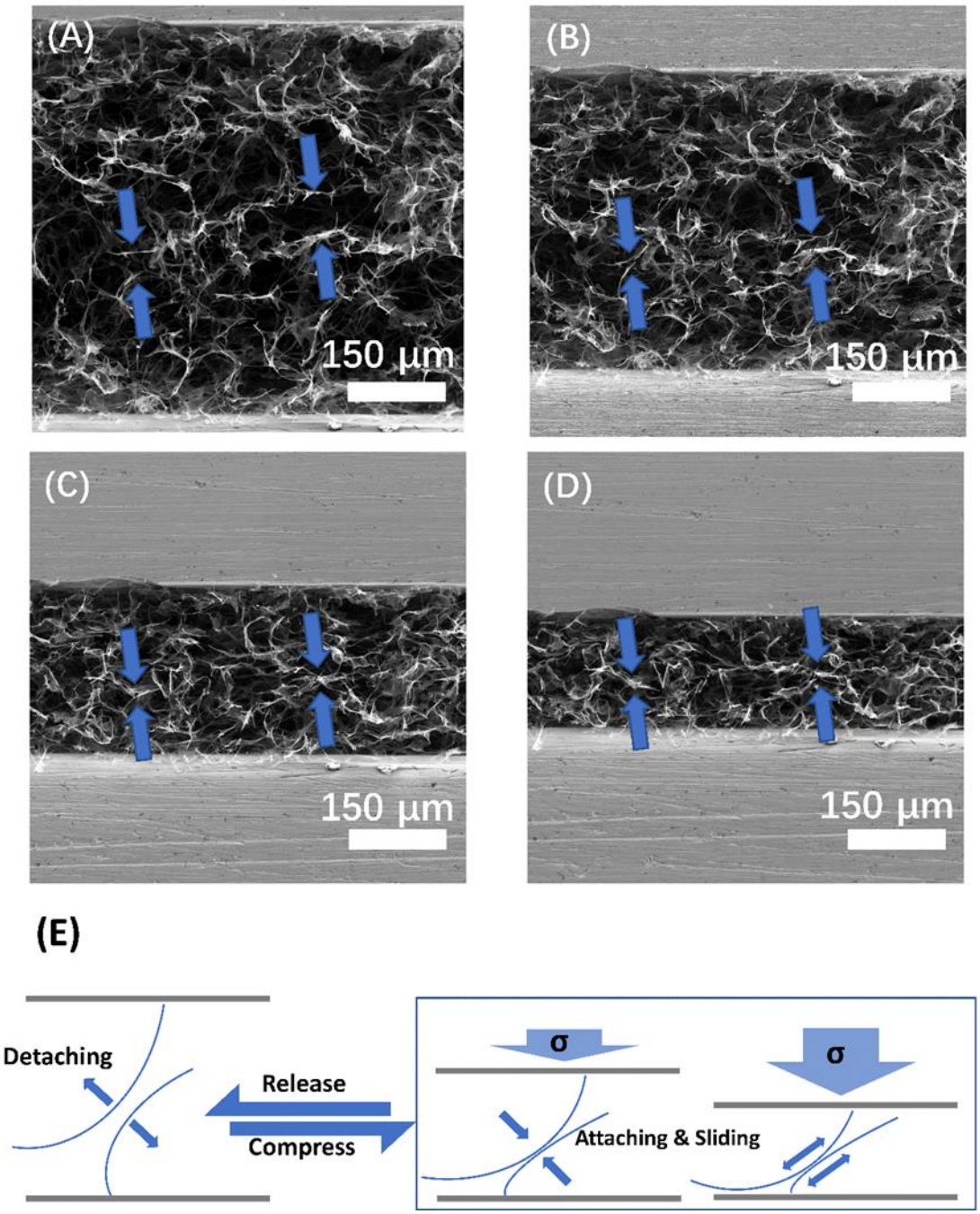

Fig. S15. Energy dissipation mechanism. (A)-(D) SEM images of the 3DGraphene foam at varying compressive strains of 0, 30, 50, and 70% respectively. The blue arrows indicate that the graphene sheets are getting closer contact upon compression. (E) Schematic illustration of detaching and attaching of graphene cell walls during compress-release process.

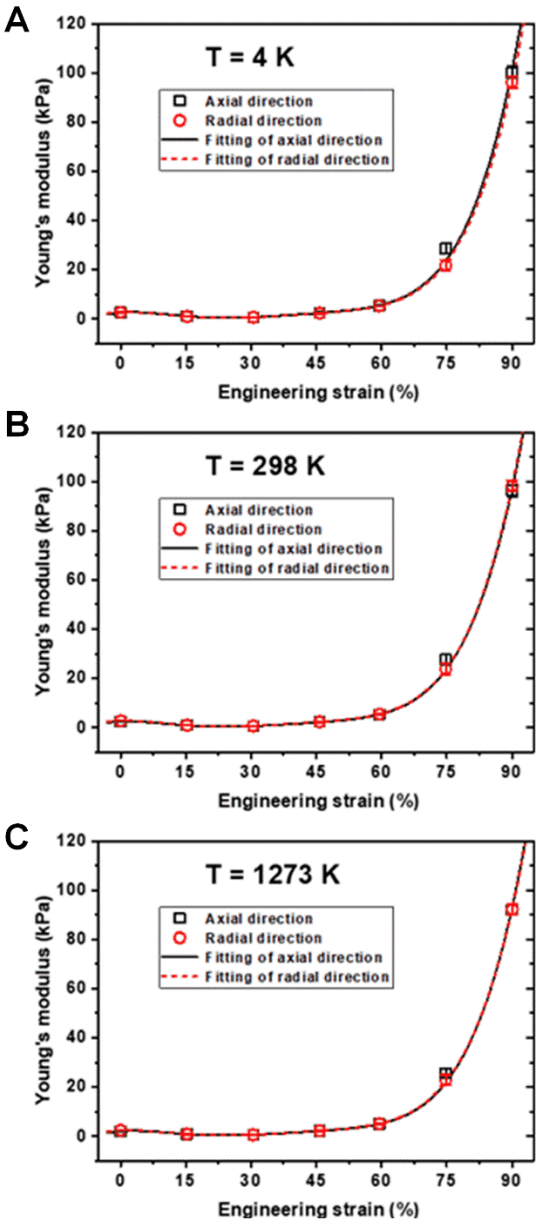

Fig. S16. Young's modulus-engineering strain plots along the axial and radial directions at different temperatures. (**A**) 4 K, (**B**) 298 K, and (**C**) 1273 K, respectively. The lines are least squares fittings and error bars represented standard deviations for the repeated measurements. The 3DGraphene foam's isotropy of Young's modulus dependency on engineering strain demonstrated temperature-invariance in wide range down to 4 K.

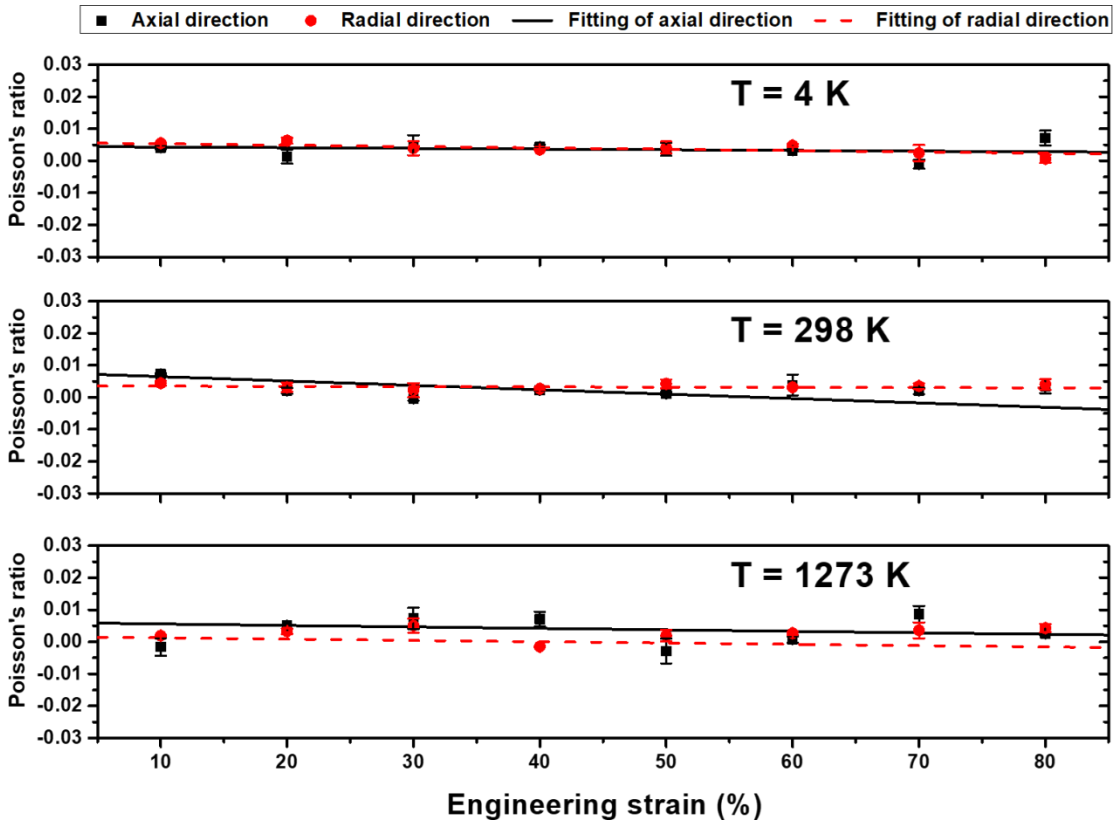

Fig. S17. Poisson's ratio at different engineering strain of the 3DGraphene foam along the axial and radial directions at different temperatures. (**A**) 4 K, (**B**) 298 K, and (**C**) 1273 K, respectively. The black solid and red dashed lines were linear fittings of the Poisson's ratio along the axial and radial directions respectively. The 3DGraphene foam demonstrated all near-zero Poisson's ratio along both axial and radial directions in wide temperature range from 4 K to 1273 K. Error bars represented standard deviations for the repeated measurements.

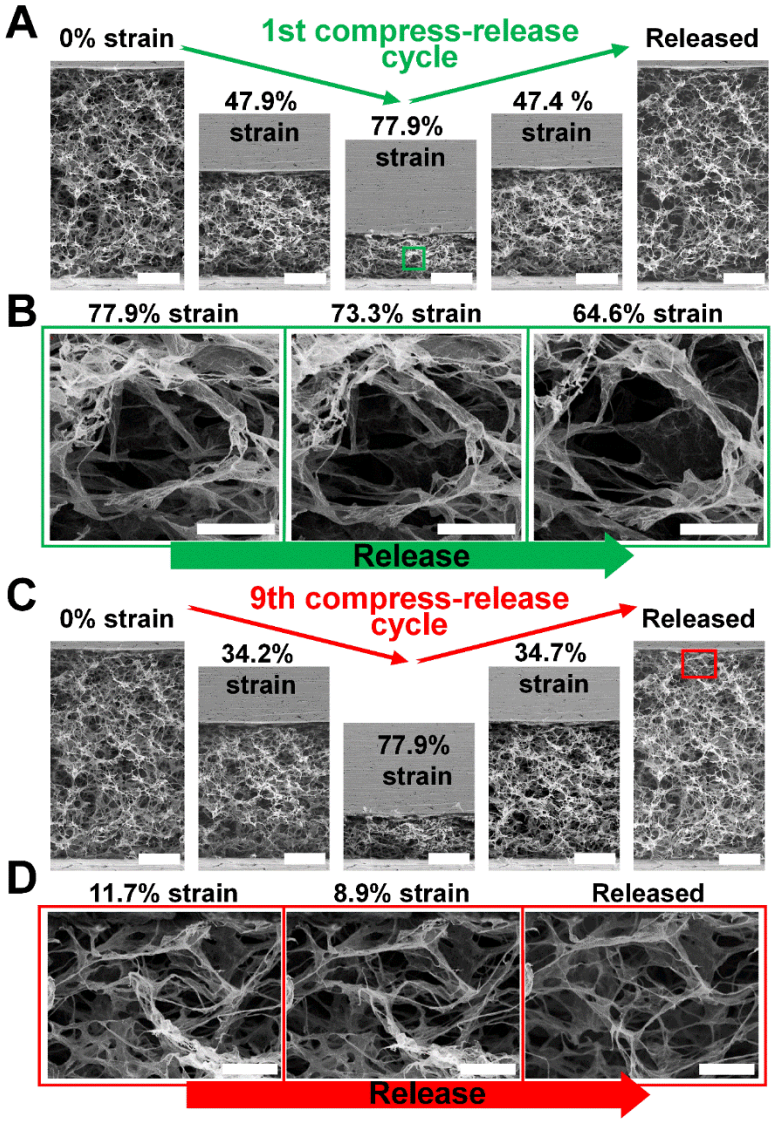

Fig. S18. In situ SEM observations of the 3DGraphene foam during compress-release cycles at 4 K. (**A**) The first cycle and (**C**) the ninth cycle, which both demonstrating the high elasticity and recoverability and great cycle stability of the microstructure even at deep cryogenic temperature. (**B**) and (**D**) are enlargements of the marked zones with decreasing compressive strains (and stresses), which both demonstrating recoverability of the deformed graphene sheets during the unloading processes. Scale bars, 100 μm in **A** and **C**, and 20 μm in **B** and **D**.

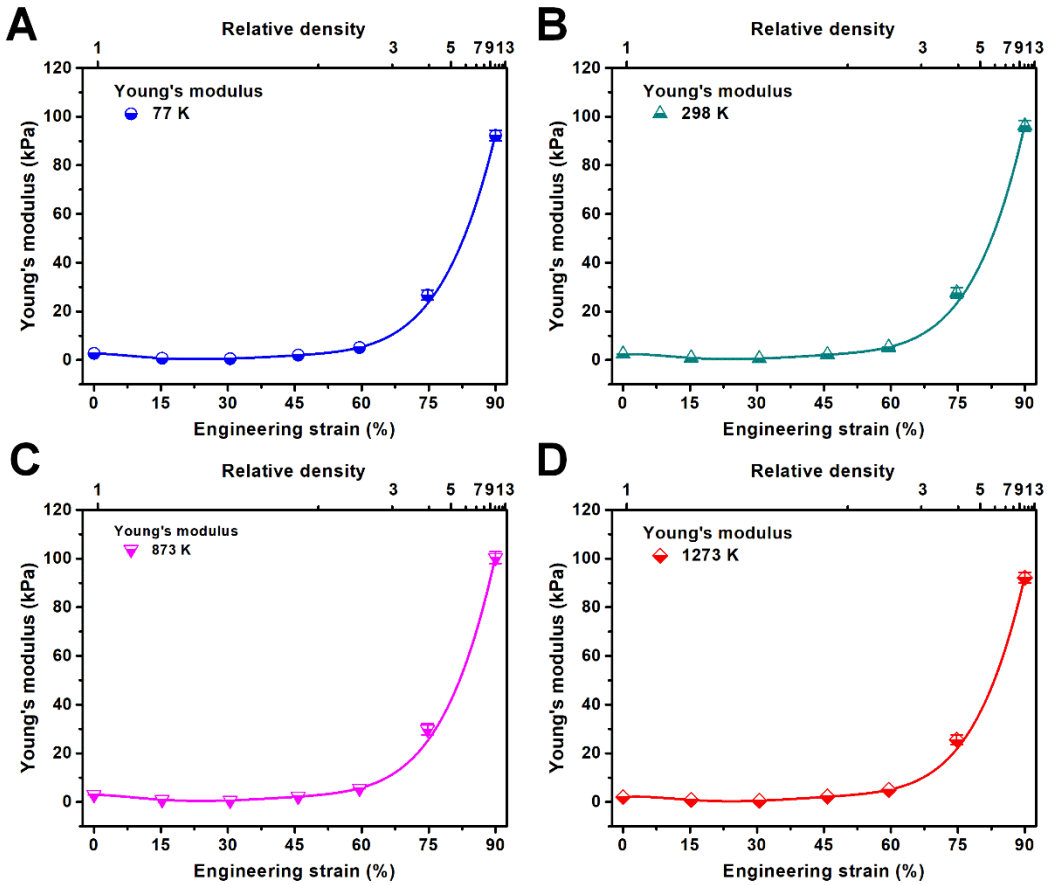

Fig. S19. The Young's modulus *versus* applied engineering strain at different temperatures. (**A**) 77 K, (**B**) 298 K, (**C**) 873 K, and (**D**) 1273 K, respectively. Error bars represented standard deviations for the repeated measurements. The solid lines were fittings of the Young's modulus with the least squares method at corresponding test temperatures.

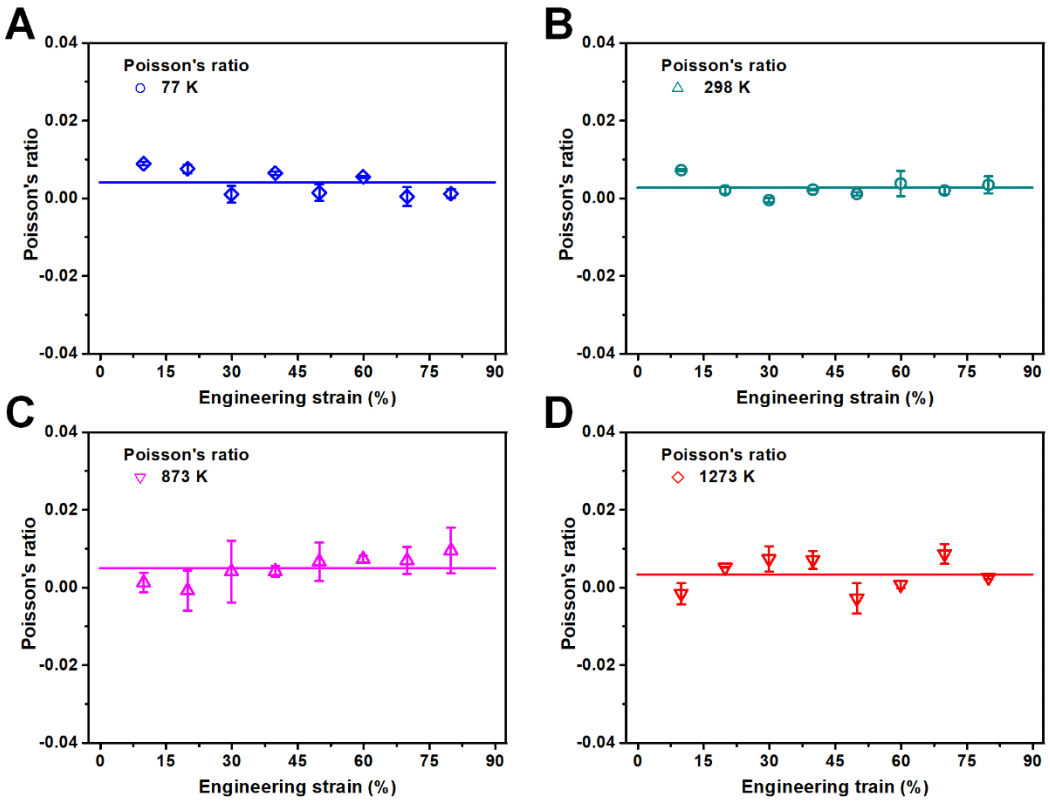

Fig. S20. The Poisson's ratio versus applied engineering strain at different temperatures. (**A**) 77 K, (**B**) 298 K, (**C**) 873 K, and (**D**) 1273 K, respectively. Error bars represented standard deviations for the repeated measurements. The solid lines were fittings of the Poisson's ratio with least squares methods at corresponding test temperatures.

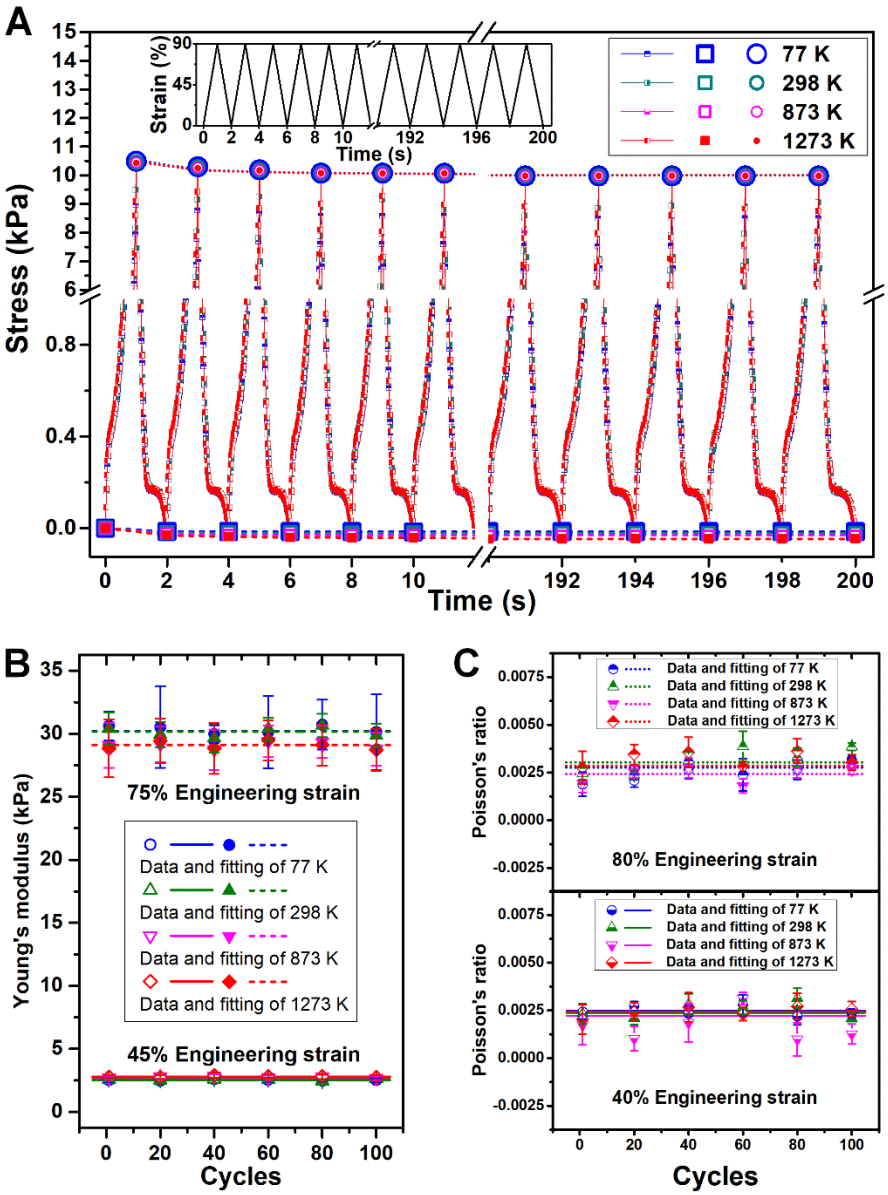

Fig. S21. The cyclic stability at different temperatures. (**A**) The stress-time curves of 100 compress-release cycles (2 seconds per cycle) along the axial direction at test temperatures of 77, 298, 873 and 1273 K. Each cycle was performed between 0% and 90% strain at 90% strain s^{-1} rate (as shown in the inset). The squares and cycles indicate the stress values at 0% and 90% strains of each cycle at a certain test temperature, and the dashed and dotted lines correspond to least squares fittings of stress at 0% and 90% strains of each temperature respectively. Almost identical and overlapping stress-time curves at different temperatures demonstrate the temperature-invariant mechanical behaviors of 3DGraphene foam. The only slight decrease of the stress at 90% strain

through several hundreds of complete cycles test from 77 K to 1273 K indicates a remarkable temperature-invariant cycle stability. (**B**) The Young's moduli at 77, 298, 873 and 1273 K (two typical groups of 45% and 75% engineering strains) kept almost unchanged during the cycling test at each temperature, showing the great cycle stability of the Young's modulus in wide temperature range. The solid and dashed lines are least squares fittings for 45% and 75% engineering strains, respectively. (**C**) The steady near-zero Poisson's ratio measured at 40% and 80% engineering strains *versus* the cycle number at 77, 298, 873 and 1273 K also show its outstanding cycle stability. The solid and dotted lines are least squares fittings for 40% and 80% engineering strains, respectively. Error bars in **B** and **C** represent standard deviations for repeated measurements of five samples.

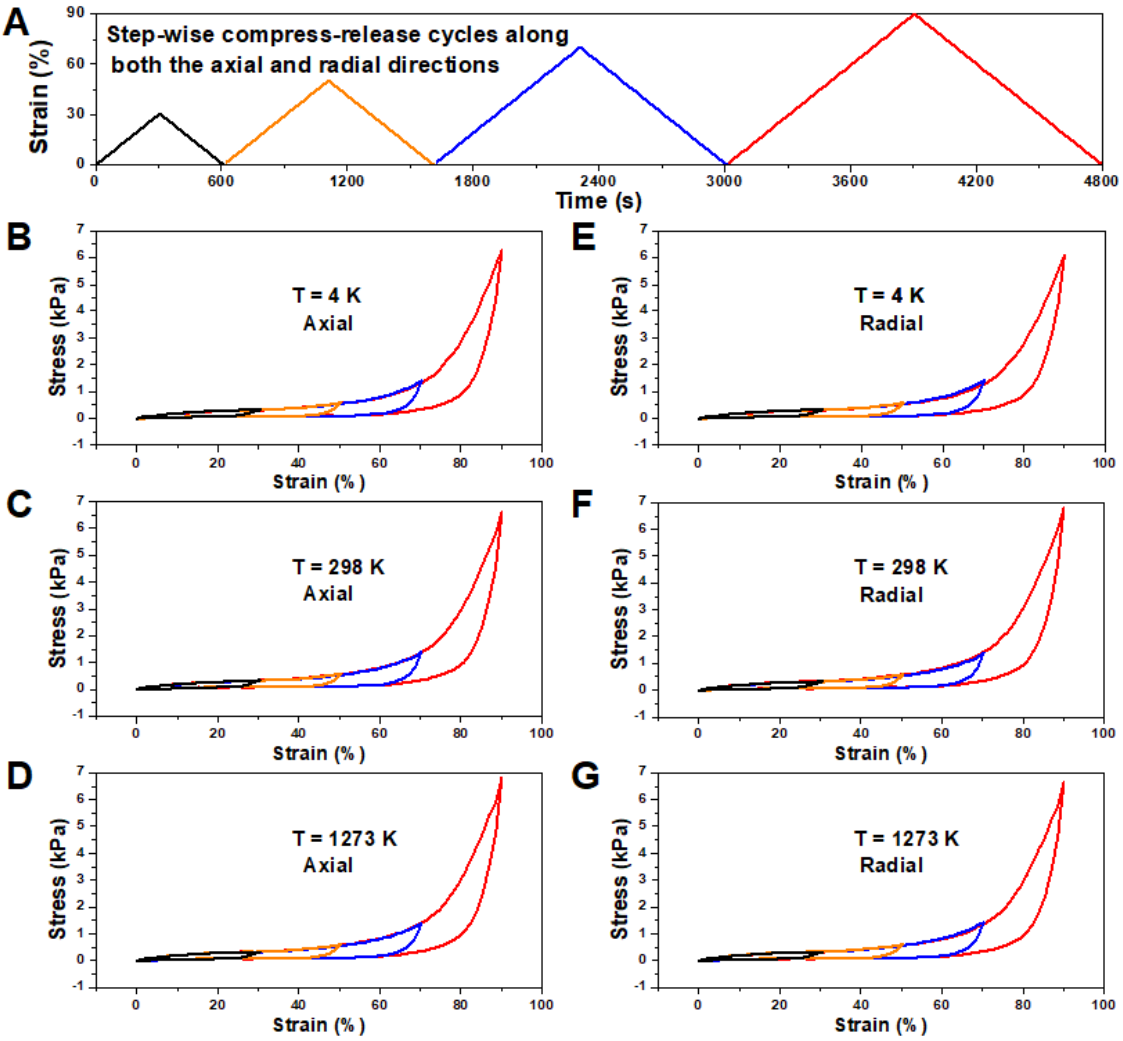

Fig. S22. The stepwise compress-release cycles with increasing maximum strain along both the axial and radial directions at different temperatures. (**A**) The strain *versus* time curve of the step-wise compress-release cycles with increasing maximum strain along both the axial and radial directions. (**B**) to (**D**) The step-wise stress-strain curves along the axial direction at 4, 298 and 1273 K, respectively. (**E**) to (**G**) The step-wise stress-strain curves along the radial direction at 4, 298 and 1273 K, respectively. The 3DGraphene foam's isotropic stress-strain behavior performed temperature independence at deep cryogenic temperature of 4 K and high temperature of 1273 K.

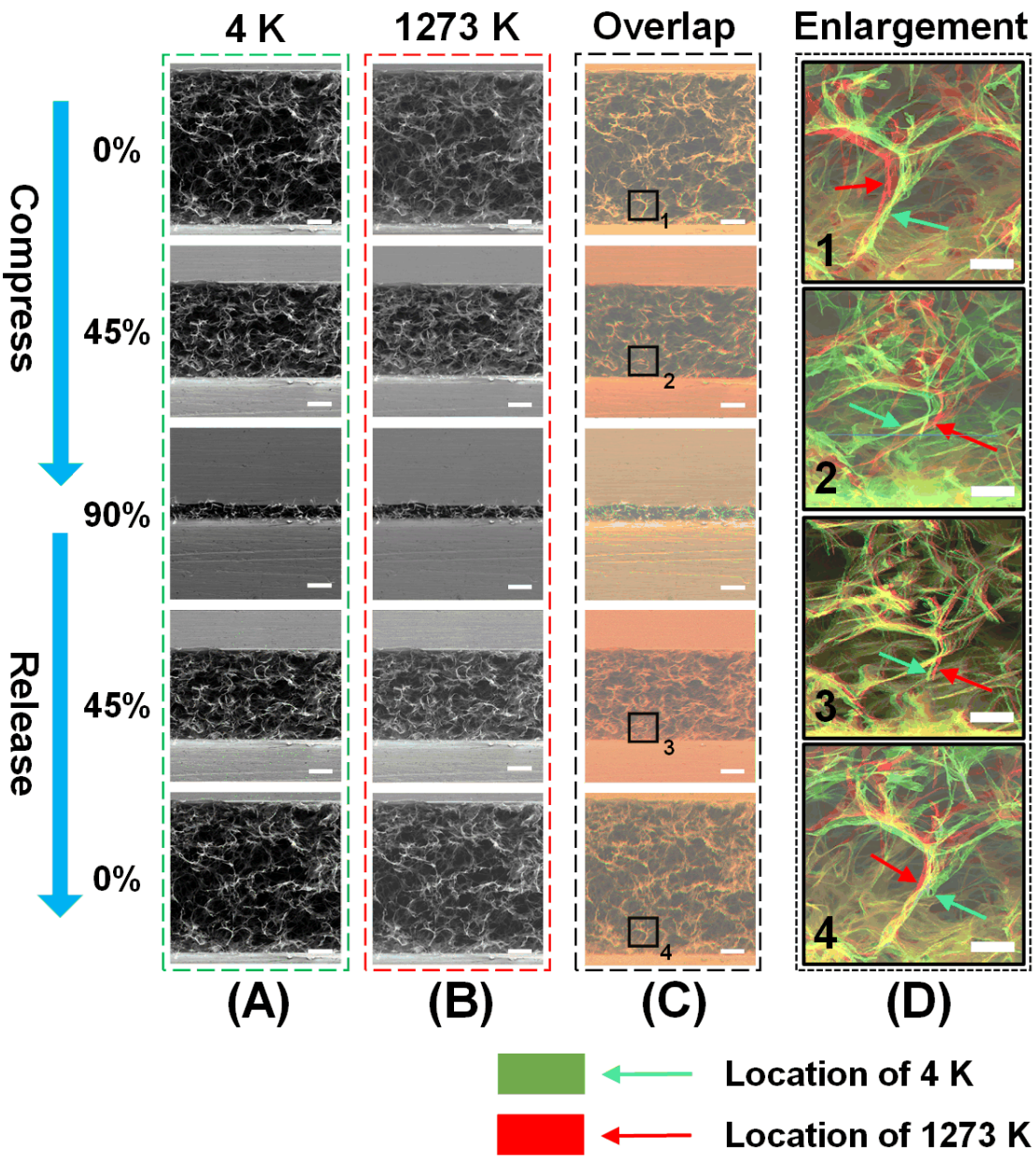

Fig. S23. Comparison of the in situ SEM images of the same sample under 0, 45, and 90% strains in the compress process. (**A**) to (**B**) *In situ* SEM images of the same sample under 0%, 45% and 90% strains in the compress process, and then released to 45% and 0% strains at 4 K (**A**) and 1273 K (**B**). (**C**) Overlaps of the images with the same strain but at different temperatures (*i.e.*, **A** and **B**), the 4 K images were processed with green color and the 1273 K images were processed with red color for clarity. (**D**) Enlargements of the labeled zones in (**C**), with green and red arrows showing the

locations of the same graphene sheets in the compress/release process at 4 K and 1273 K. Scale bars, 100 μm in **A-C**, and 25 μm in **D**.

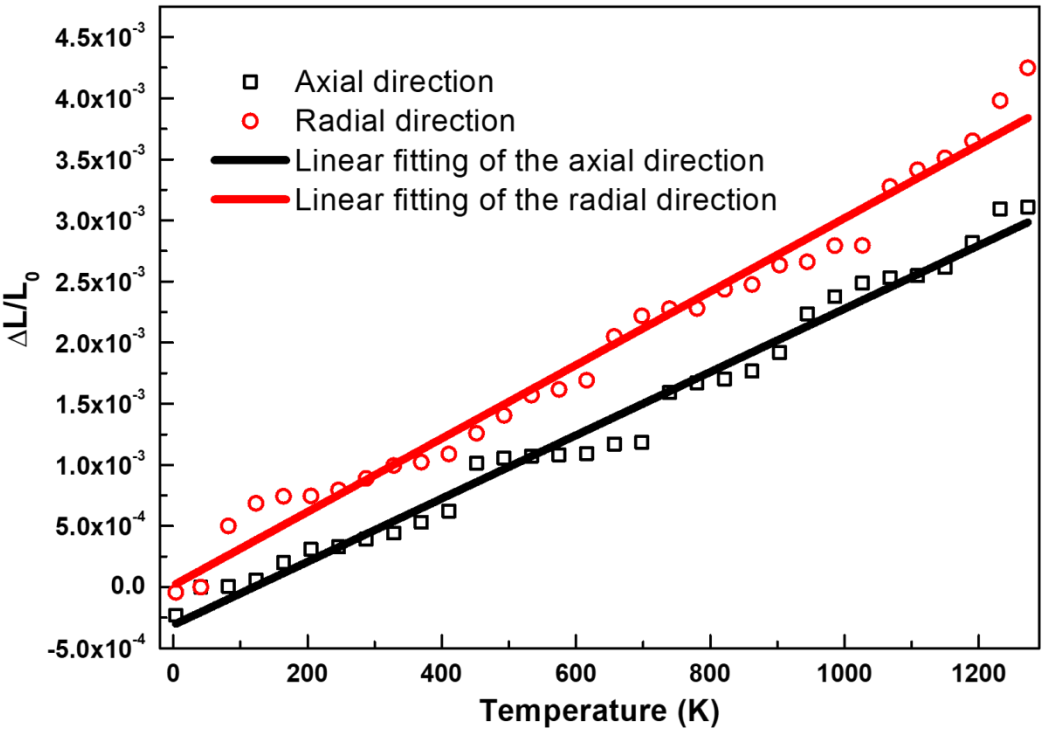

Fig. S24. Thermal expansion of the 3DGraphene foam in both axial and radial directions. The isotropic 3DGraphene foam demonstrated very small and nearly identical thermal expansion coefficients between 4 K and 1273 K, which were 2.6 × 10^{-6} K^{-1} and 3.0 × 10^{-6} K^{-1} for the axial and radial directions, respectively.

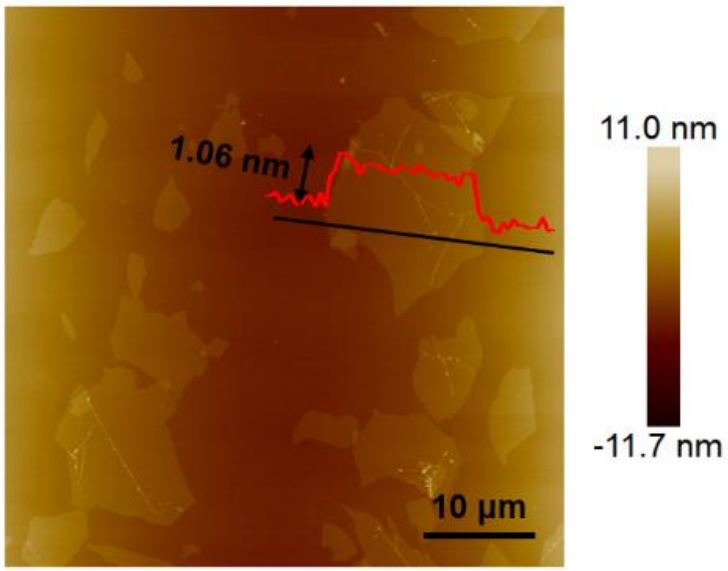

Fig. S25. A typical AFM image of GO sheets. The 3DGraphene foam was prepared from a GO ethanol solution of 0.5 mg ml^{-1}. The height difference between the steps was 1.06 nm, indicating the typical step height of an individual single layer GO sheet.

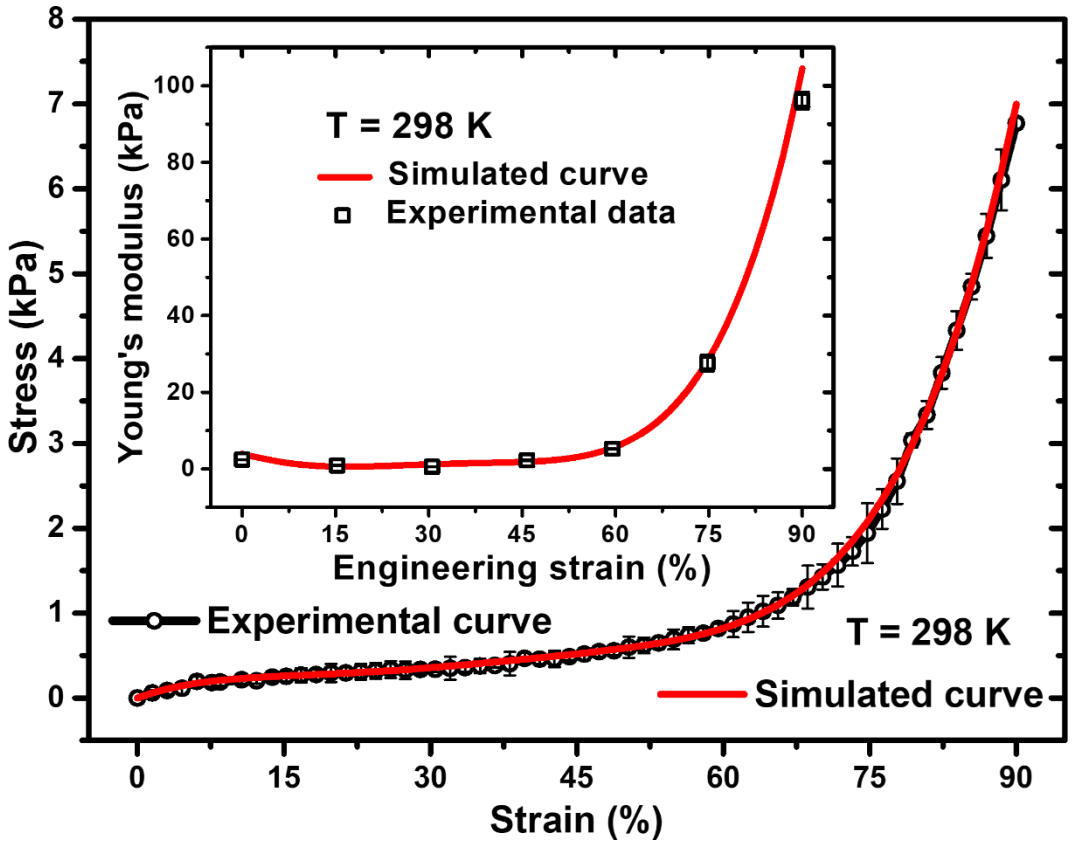

Fig. S26. The simulated stress-strain curve at 298 K. The theoretically simulated stress-strain curve agrees well with the experimental result for the compression of 3DGraphene foam at 298 K. Inset shows the simulated Young's modulus-engineering strain curve agreeing well with the experimental data at 298 K. Error bars represent standard deviations for the repeated measurements.

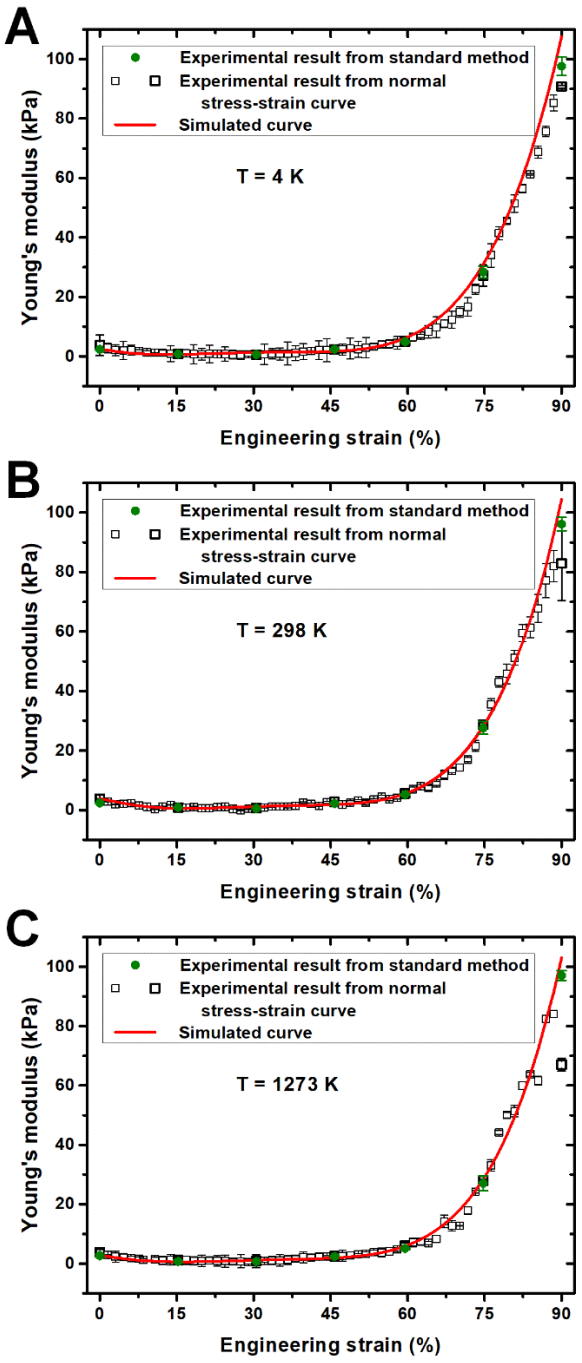

Fig. S27. The simulated Young's modulus–engineering strain curves at different temperatures. (**A**) to (**C**) The experimental Young's modulus-engineering strain results (black hollow squares) from the normal stress-strain curves (with 0.1% strain s^{-1} between 0% and 90% strain) and from the standard method (green solid circles) at 4 K (**A**), 298 K (**B**) and 1273 K (**C**). The red lines were the theoretically simulated Young's modulus-engineering strain curves at 4 K, 298 K and 1273 K, respectively. Error bars

represented standard deviations for the repeated measurements of five samples with five times for each one.

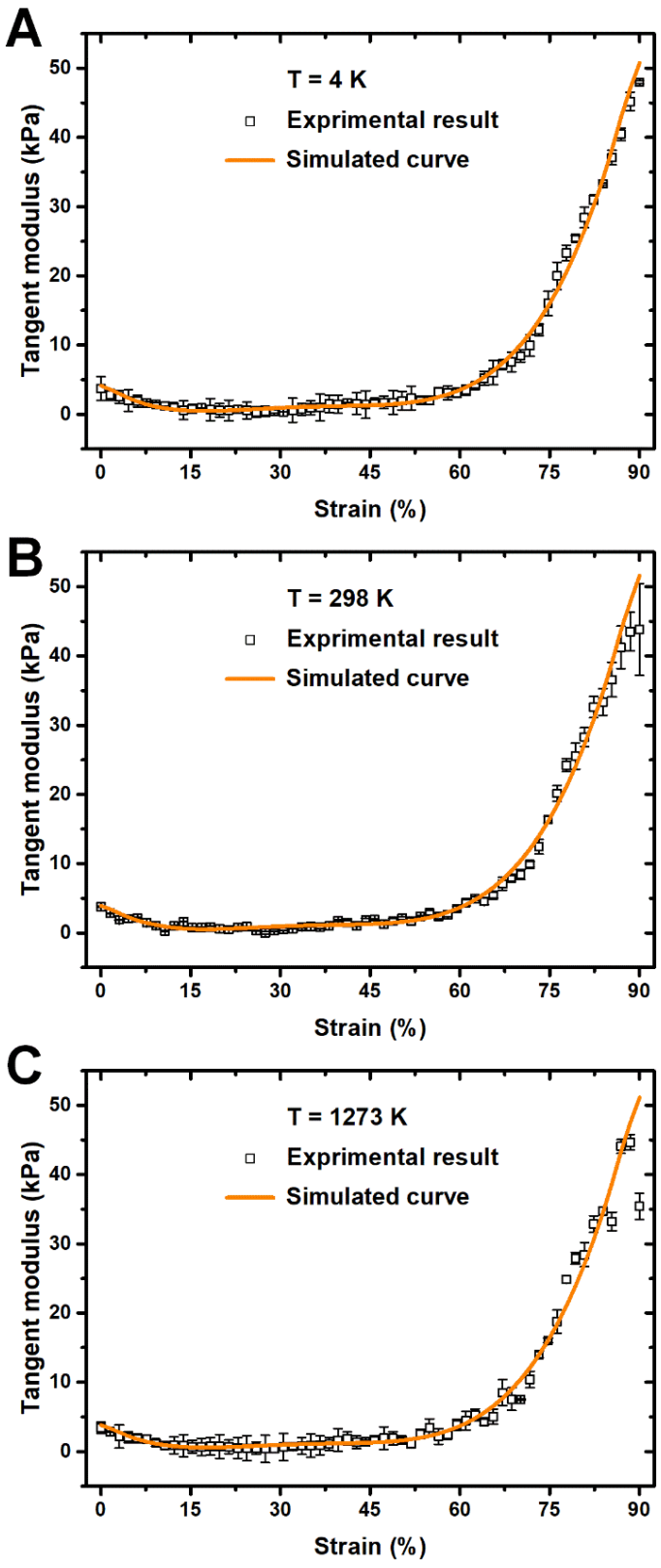

Fig. S28. The simulated tangent modulus–strain curves at different temperatures. (**A**) to (**C**) The theoretically simulated tangent modulus-strain curves (yellow lines) and the experimental results which were obtained from the normal stress-strain curves with

0.1% strain s^{-1} between 0% and 90% strain at 4 K (**A**), 298 K (**B**) and 1273 K (**C**). Error bars represented standard deviations for the repeated measurements of five samples with five times for each one.

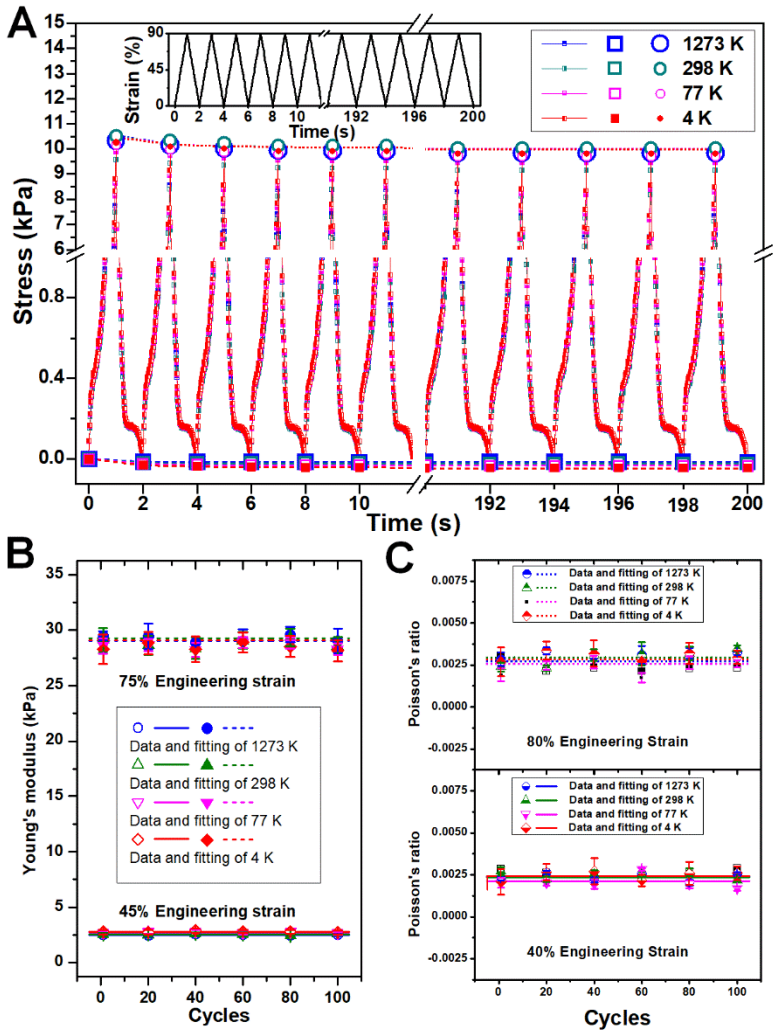

Fig. S29. Results of cyclic mechanical test at 1273 K and that of the following test at other temperatures for the same samples. (**A**) The stress-time curves of 100 compress-release cycles (2 seconds per cycle) along the axial direction at test temperatures of 1273, 298, 77 and 4 K. Each cycle was performed between 0% and 90% strain at 90% strain s^{-1} rate (as shown in the inset). The squares and cycles indicate the stress values at 0% and 90% strains of each cycle at a certain test temperature, and the dashed and dotted lines correspond to least squares fittings of stress at 0% and 90% strains of each temperature respectively. Almost identical and overlapping stress-time curves at different temperatures demonstrate the almost unchanged mechanical behaviors of 3DGraphene foam after high temperature tests. (**B**) The Young's modulus at 1273, 298, 77 and 4 K (two typical groups of 45% and 75% engineering strains) kept almost unchanged during the cycling test at each temperature, showing the great thermal stability of the Young's modulus after high

temperature tests. The solid and dashed lines are least squares fittings for 45% and 75% engineering strains, respectively. (**C**) The steady near-zero Poisson's ratio measured at 40% and 80% engineering strains *versus* the cycle number at 1273, 298, 77 and 4 K also show its outstanding thermal stability after high temperature tests. The solid and dotted lines are least squares fittings for 40% and 80% engineering strains, respectively. Error bars in **B** and **C** represent standard deviations for repeated measurements of five samples.

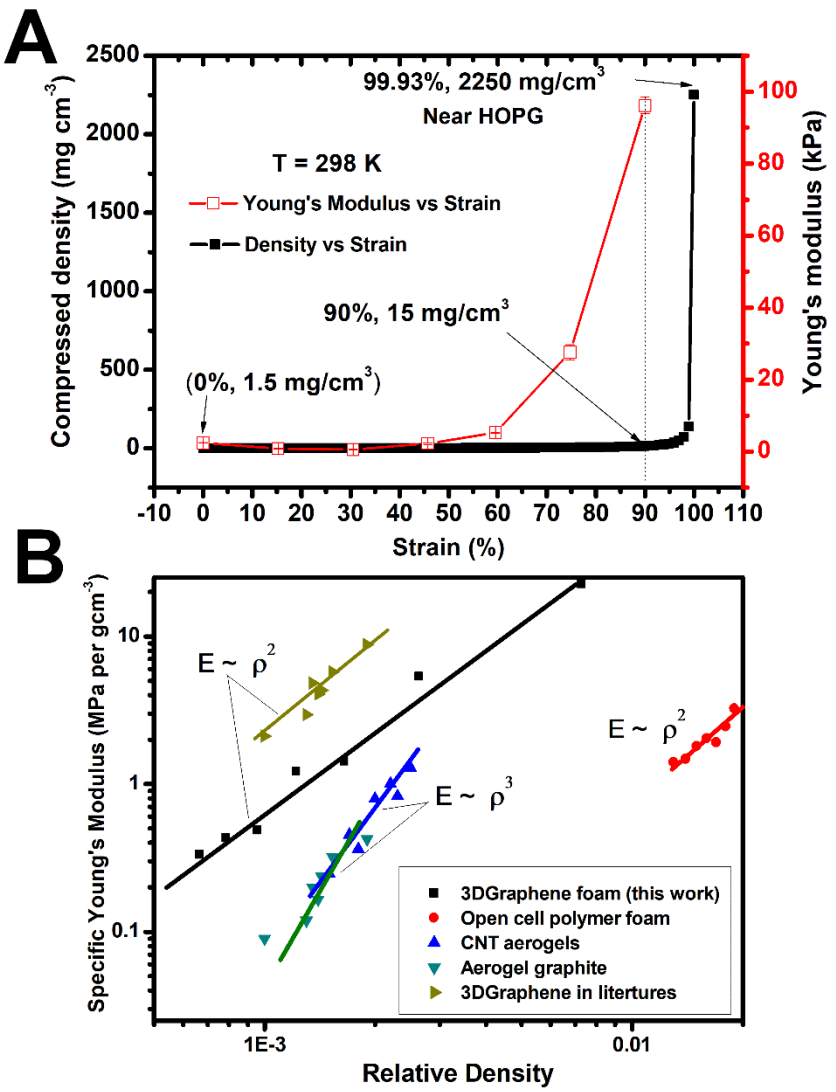

Fig. S30. The relationship between compressed density and Young's modulus with strain. (**A**) The measured Young's Modulus increase with compressive strain (at 298 K), and the same for the density, as shown by the hollow red points. When compressed to 90 % strain, the Young's modulus reaches near ~100 kPa. At the upper limit compression strain near 100%, the density reaches the ideal value of HOPG 2.25 g cm^{-3}. (**B**) Comparison of the modulus-density relationship of varies cellular materials.

Captions for Movies S1 to S4

Movie S1. In situ optical observation for compress-release cycles of the 3DGraphene foam at 4 K and corresponding stress-strain transient curves. *In situ* optical observation using endoscope for compress-release cycles of 3DGraphene foam at 4 K, from 0% to 90% strain at a rate of 50% strain s^{-1}, for three complete cycles and one cycle with 10 s pause, which showed the highly reversible compressive elasticity and no brittleness of the 3DGraphene foam at such an extremely low temperature. Attached panel on the right side demonstrated the corresponding stress-strain curves of the whole process. The sample was 15 mm in both diameter and height, as indicated by the ruler next to the sample and the scale bar.

Movie S2. In situ optical observation for compress-release cycles of the 3DGraphene foam at 1273 K and corresponding stress-strain transient curves. *In situ* optical observation using endoscope for compress-release cycles of 3DGraphene foam at 1273 K, from 0% to 90% strain at a rate of 50% strain s^{-1}, for three complete cycles and one cycle with 10 s pause, which showed the highly reversible compressive elasticity and no breakdown of the 3DGraphene foam at such a high temperature. Attached panel on the right side demonstrated the corresponding stress-strain curves of the whole process. The sample was 15 mm in both diameter and height, as indicated by the ruler next to the sample and the scale bar. The color deviation of the video was conducted by the high temperature radiation.

Movie S3. In situ SEM observation for compress-release cycles of the 3DGraphene foam at 4 K. In situ SEM observation of the 3DGraphene foam (with 600 μm length along the compression direction) in the compress-release cycles at 4 K, from 0% to 90% strain with 15% strain each step. The scale bar in the video was 100 μm. The microscopic structure of the 3DGraphene foam was almost completely reversible without obvious structural change through the compress-release process at such a deep cryogenic temperature. The elastic bending/buckling deformation of single graphene sheet during compress-release process of the material at such a deep

cryogenic temperature could also be observed directly. All these indicated the high elasticity (without harden and brittleness) of both the graphene building block and the overall material.

Movie S4. In situ SEM observation for compress-release cycles of the 3DGraphene foam at 1273 K. *In situ* SEM observation of the 3DGraphene foam (the same one of Supplementary Video 3, with 600 μm length along the compression direction) in the compress-release cycles at 1273 K, from 0% to 90% strain with 15% strain each step. The scale bar in the video was 100 μm. The microscopic structure of the 3DGraphene foam was almost completely reversible without obvious structural change through the compress-release process at such a high temperature. The elastic bending/buckling deformation of single graphene sheet during compress-release process of the material at such a high temperature could also be observed directly. All these indicated the high elasticity (without soften and breakdown) of both the graphene building block and the overall material.